ANISOTROPIC ASPECTS OF HEAVY QUARKONIUM POTENTIAL IN THERMAL QCD MEDIUM

By

JOBIN SEBASTIAN

PHYS11201704015

National Institute of Science Education and Research, Bhubaneswar

A thesis submitted to the

Board of Studies in Physical Sciences

In partial fulfillment of requirements

for the Degree of

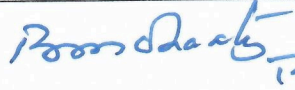**DOCTOR OF PHILOSOPHY**
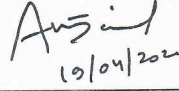
of

HOMI BHABHA NATIONAL INSTITUTE

December, 2023

Homi Bhaba National Institute

Recommendations of the Viva Voce Committee

As members of the Viva Voce Committee, we certify that we have read the dissertation prepared by Jobin Sebastian entitled "Anisotropic Aspects of Heavy Quarkonium Potential in Thermal QCD Medium" and recommend that it may be accepted as fulfilling the thesis requirement for the award of Degree of Doctor of Philosophy.

Chairman -	Prof. Bedangadas Mohanty		19/4/2024
Guide / Convener -	Dr. Najmul Haque		19.04.2024
Examiner -	Prof. Michael Strickland		19/04/2024
Member 1 -	Dr. Amaresh Kumar Jaiswal		19/04/2024
Member 2 -	Dr. Victor Roy		19.04.24
Member 3 -	Dr. Sandeep Chatterjee		19/04/2024

Final approval and acceptance of this thesis is contingent upon the candidate's submission of the final copies of the thesis to HBNI.

I hereby certify that I have read this thesis prepared under my direction and recommend that it may be accepted as fulfilling the thesis requirement.

Date : 19.04.2024

Place : Jatni

Dr. Najmul Haque (Guide)

i

STATEMENT BY AUTHOR

This dissertation has been submitted in partial fulfillment of requirements for an advanced degree at Homi Bhabha National Institute (HBNI) and is deposited in the Library to be made available to borrowers under rules of the HBNI.

Brief quotations from this dissertation are allowable without special permission, provided that accurate acknowledgement of source is made. Requests for permission for extended quotation from or reproduction of this manuscript in whole or in part may be granted by the Competent Authority of HBNI when in his or her judgment the proposed use of the material is in the interests of scholarship. In all other instances, however, permission must be obtained from the author.

Jobin Sebastian

DECLARATION

I hereby declare that I am the sole author of this thesis in partial fulfillment of the requirements for a postgraduate degree from National Institute of Science Education and Research (NISER). I authorize NISER to lend this thesis to other institutions or individuals for the purpose of scholarly research.

Jobin Sebastian

List of Publications arising from the thesis

Journal

1. "Liénard-Wiechert potential of a heavy quarkonium moving in QGP medium", **Jobin Sebastian**, Mohammad Yousuf Jamal, and Najmul Haque, Phys.Rev.D 107 (2023) 5, 054040.

2. "Heavy quarkonia in QGP medium in an arbitrary magnetic field", **Jobin Sebastian**, Lata Thakur, Hiranmaya Mishra, and Najmul Haque, Phys.Rev.D 108 (2023) 9, 094001.

Conferences

1. 8th International Conference on Physics and Astrophysics of Quark Gluon Plasma (ICPAQGP-2023), 7-10 February 2023, Odisha, India.

2. Particles and Nuclei International Conference (PANIC 2021), 5 - 10 Sep 2021, Lisbon, Portugal.

3. DAE-BRNS symposium on Contemporary and Emerging Topics in High Energy Nuclear Physics (CETHENP 2022), VECC, Kolkata, India, November 15-17, 2022.

4. DAE-BRNS Symposium on High Energy Physics, NISER, Bhubaneswar, India, December 14-18, 2020.

5. DAE-BRNS symposium on Contemporary and Emerging Topics in High Energy Nuclear Physics (CETHENP 2019), VECC, Kolkata, India, November 25-27, 2019.

Others

1. "Stability and causality of the relativistic third order hydrodynamics", **Jobin Sebastian**, PoS PANIC2021, 250 (2022).

Jobin Sebastian

Dedicated

to the

Indian heavy ion community

"Where the mind is without fear and the head is held high;
Where knowledge is free;
Where the world has not been broken up into fragments by narrow domestic walls;
Where words come out from the depth of truth;
Where tireless striving stretches its arms toward perfection;
Where the clear stream of reason has not lost its way into the dreary desert sand of dead habit;
Where the mind is led forward by thee into ever-widening thought and action -
Into that heaven of freedom, my Father, let my country awake."

\- Tagore, Gitanjali

ACKNOWLEDGEMENTS

ABSTRACT

Quarkonia are bound states of heavy quarks (such as charm and bottom quarks), and their antiquarks hold a prominent significance in the study of the quark-gluon plasma (QGP) created in heavy-ion collision experiments. Their importance stems from their unique characteristics in the extreme environment of a hot and dense plasma of quarks and gluons. Quarkonia are predominantly produced in the very early stages of the heavy ion collision due to their higher masses, and they subsequently behave almost independently as they transit the various phases of the QGP. Their behavior is largely explained by the potential model, which accounts for the interaction between quark and antiquark pairs within the QGP medium. This potential model is a cornerstone of our understanding of the properties of the thermal medium, as it allows us to infer crucial information about the medium temperature and screening effects. By studying quarkonium-bound states in the QGP medium using the potential model formalism, we gain valuable insights into the QGP characteristics, allowing us to unravel the fundamental nature of matter at extreme conditions and contributing to our understanding of the early universe evolution. Matsui and Satz first suggested the concept of heavy quarkonium suppression in QGP, highlighting the Debye screening effect as a key factor in weakening the quark-antiquark interaction. This thesis explores the anisotropic aspects of Debye screening and quarkonium potential arising due to the relative motion between quarkonia and the thermal medium and the presence of strong magnetic fields resulting from noncentral nuclear collisions.

The characteristics of the complex potential of a uniformly moving heavy quarkonium through a hot and dense static QGP medium are investigated. The well-known notion of the retarded potential in electrodynamics is extended to the context of the heavy quarkonia by altering the static vacuum Cornell potential through Lorentz transformation to the static frame of the QGP medium. The resulting potential in the vacuum is also corrected using the medium dielectric permittivity to incorporate the Debye screening effect offered by the QGP medium. To study the effect of the magnetic field, the one-loop gluon polarization tensor is obtained in the presence of an external, constant, and homogeneous magnetic field employing the Schwinger proper time formalism in Euclidean space. The gluon propagator is calculated from the gluon polarization tensor and is used to calculate the dielectric permit-

tivity in the presence of the magnetic field. The modified dielectric permittivity is then used to compute the heavy quarkonium complex potential in static QGP. This research reveals that the quarkonium potential exhibits an anisotropic nature, and it depends on the angle between the quark-antiquark dipole axis and the direction of velocity and/or the magnetic field direction. The velocity dependence and effect of the magnetic field on the quarkonium potential and the thermal width are presented. The discussion includes numerical results for both the real and imaginary components of the potential, accompanied by an examination of the analytical expression of the potential, approximated under the constraint of a small velocity limit. Further, the limitation of the strong-field approximation, as done in literature in the light of heavy-ion observables, is discussed as the effect of the magnetic field is very nominal to the quarkonium potential.

Contents

Summary

We have examined the potential of a moving heavy quarkonium in a static QGP medium in this thesis. Using the analogy of the Liénard-Wiechert potential in electrodynamics, where the static potential is transformed using Lorentz transformation to find its form in a boosted frame, we first derived the retarded potential of a uniformly moving heavy quark in the vacuum. The resulting velocity and angular-dependent potential are then modified for the inclusion of the Debye screening effect. The medium dielectric permittivity, a complex quantity that results in a complex potential, has been used to accomplish this. Exact numerical results are presented in the thesis, and the analytical expression for the real and imaginary parts of the potential is derived in the small velocity limit. We have shown how the potential varies with respect to a number of parameters, including temperature, velocity, angular dependence, and the quark-antiquark distance. Additionally, taking into account the existence or absence of string terms, we have provided a comparison between the Cornell and Coulombic potentials. It is found that the string term dominates at a large quarkonium separation distance, while the Coulombic contribution is dominated at a short distance. Next, it is found that the anisotropy of the potential increases with increasing velocity and that the spherical symmetry of the potential is broken by the motion of quarkonium through the QGP. It has also been observed that the potential's velocity dependence is just as significant as its temperature dependence. It turns out that the direction of motion of quarkonium is where the real and imaginary parts of the potential from the corresponding static case vary the most. At last, we determined the thermal width, which rises with temperature and falls with velocity. This indicates that the velocity of quarkonium and the medium temperature control the lifetime of a quarkonium-bound state.

Additionally, we have assessed the influence of a magnetic field on the heavy quarkonium complex potential. Firstly, we calculated the dielectric permittivity from the static limit of the gluon propagator. The one-loop gluon self-energy in the presence of an external magnetic field was used to derive this propagator in Euclidean space using Schwinger proper time formalism. The quark-loop contribution to the gluon self-energy and coupling

constant allows the magnetic field to enter the formalism. Then, we used the modified dielectric permittivity to compute the in-medium heavy quarkonium complex potential. Results showed that this potential becomes anisotropic and changes with magnetic field strength and angle Θ between the quark-antiquark axis and the direction of the magnetic field. At very high magnetic field strengths, the real part of the potential gets flattened due to an increase in screening with eB. On the other hand, the imaginary part of the quarkonium potential undergoes a rise in magnitude at short distances, followed by a decrease at long distances. Finally, we observed that the overall effect of the magnetic field on the complex potential is rather small for any realistic magnitudes of the magnetic field generated in heavy ion collisions. We computed the thermal widths of the ground and first excited states of bottomonium (Υ, Υ') and charmonium (J/ψ, ψ') utilizing the imaginary part of the potential. We found that the excited states (Υ', ψ') are more sensitive to the magnetic field than the ground states (Υ, J/ψ). The effect of magnetic fields decreases with increasing heavy quark mass and decreasing size, making the charmonium states more susceptible to magnetic field strength than the bottomonium states. For the decay widths, as the temperature increases, the sensitivity to magnetic fields decreases, eventually disappearing at high temperatures. We have further compared our results with the strong-field approximated potential. We found that such an approximated potential does not even come close to the potential without such an approximation for any realistic magnetic field value generated in heavy ion collisions. This invalidates the strong magnetic field approximation usually adopted in literature for the heavy quarkonium complex potential. For the realistic strengths of magnetic fields, one needs to more general treatment, as has been attempted here. Also, it should be mentioned that new divergences in the gluon propagators are introduced by the weak-field expansion, and this requires regulation.

List of Figures

Chapter 1

Introduction

1.1 A brief history

In the annals of modern physics, the early 1970s marked a pivotal period when the nature of the strong force, one of the fundamental interactions governing the universe, was unveiled. The development of Quantum Chromodynamics (QCD), a non-Abelian gauge theory that concisely captured the complexities of the strong force, served as the trigger for this shift. Exactly 50 years ago, three important papers were published in 1973 by David J. Gross and Frank Wilczek [1, 2], and H. David Politzer [3], establishing a crucial turning point in our comprehension of the strong force. The breakthrough idea of asymptotic freedom, a cornerstone of QCD, was founded in these works. Asymptotic freedom was the profound revelation that the coupling constant of the strong force decreases at high-energy scales, rendering high-energy QCD processes perturbatively calculable. On the other hand, the coupling constant rises at low energies, which accounts for the observed confinement of quarks, one of the most mysterious phenomena in particle physics.

This was an era where the search for the strong force was entwined with an expanding particle zoo that went beyond the protons and neutrons that make up atomic nuclei. Physicists were bewildered by this zoo's ever-growing collection of particles, all of which were thought to be elementary. The theoretical framework that eventually brought order to this chaotic ensemble was the "eightfold way," an organizational structure drawn from the SU(3) group representations [4]. This remarkable construct provided a successful ordering of hadrons and predicted the existence of the omega baryon, which had been discovered

in 1964. Within this theoretical framework, the notion of quarks, elementary constituents of hadrons, was born. The three flavors of quarks, up, down, and strange, were postulated to support the intricacy of hadron structure [5]. To address the problem of constructing specific hadrons while respecting the spin-statistics, a new quantum number called "color" was attributed to the quarks [6, 7].

While the quark model provided sophisticated grounds for the observed hadrons, the physical reality of these elementary particles remained purely theoretical [8]. The introduction of the SLAC-MIT deep-inelastic scattering experiments, which involved electron collisions with proton targets, marked the turning point [9, 10]. These investigations revealed a scaling relation that could only be explained by presuming that the electrons scattered off by pointlike non-interacting fermion constituents within the protons: the quarks. It was a significant step towards confirming the existence of quarks as the fundamental building blocks of matter [11–13].

With the emergence of quarks, it became apparent that the strong nuclear force accountable for holding the quarks together within protons and other hadrons was surprisingly weak at distances shorter than the radius of protons [14–16]. The need for a comprehensive theory to explain this phenomenon, known as asymptotic freedom, was imperative. The blueprint for this effort was found in Yang-Mills theory [17], a framework earlier successful in describing the electroweak force. In 1973, Gross, Wilczek, and Politzer unveiled the distinctive property, asymptotic freedom, of SU(3) Yang-Mills theory. This theoretical framework, where quarks interact through the exchange of gluons, bore the name Quantum Chromodynamics (QCD) and emerged as the backbone of the strong force [18].

A notable empirical anomaly of QCD was the absence of isolated colored quarks and gluons in nature. Kenneth Wilson offered a compelling explanation for this mystery, demonstrating that SU(3) Yang-Mills theory yields an attractive potential that linearly increases with the distance between quarks, thereby confining them [19]. Wilson's work also intro-

duced the revolutionary concept of lattice gauge theory, a tool instrumental in understanding the low-energy behavior of QCD [20]. The first numerical simulations of SU(2) QCD, based on lattice gauge theory and verifying the coexistence of confinement and asymptotic freedom within a single theoretical framework, were carried out by 1980, largely due to the efforts of Creutz [21]. The potential of quantum computer simulations of QCD, made possible by Kogut and Susskind's Hamiltonian formulation of the lattice gauge theory, opens up new avenues for investigation in this complex field [22].

A promising discovery in November 1973 confirmed the existence of the charm quark, which was postulated by the consistency of electroweak interactions. A striking resonance peak observed in electron-positron collisions at Brookhaven National Laboratory and Stanford Linear Accelerator Center (SLAC) revealed the existence of the J/ψ particle [23–25]. This newly discovered quark species provided a convincing explanation of the J/ψ as a bound state of charm and anticharm quarks, like the hydrogen atom, bound together by the strong force (more about this particle in the context of QGP is the main topic of discussion in this thesis). After that, the "top" and the "bottom" quarks were discovered, which added to the particle spectrum's richness and also added a source of CP violation to the standard model [26–28]. These findings demonstrated how our knowledge of quark matter and its crucial function in the subatomic universe is constantly changing.

On the other hand, the fundamental assumption of QCD is that the gluons are the carriers of the strong force. This idea is hampered by the fact that gluons are color-charged particles whose confinement prevents direct detection. Experimental confirmation of the spin-1/2 nature of quarks was achieved by detecting correlations in back-to-back hadronic jet events. Observing three coplanar jets of hadrons arising from an underlying emission of a quark, an antiquark, and a gluon, investigations at the PETRA collider at DESY built upon this and marked a significant breakthrough [29–33]. This revealed the existence of gluons for the first time, although only indirectly, and clarified the mysterious nature of the strong force

carriers.

The spontaneous breaking of global symmetries emerged as a fundamental concept in particle physics, resulting in massless Goldstone bosons. The classical version of QCD with nearly massless light quarks has an approximate global $SU_L(2) \times SU_R(2) \times U(1) \times U(1)$ chiral symmetry that rotates the up-down quark flavors and the left-right chiralities. Particularly, the vacuum of QCD spontaneously breaks this global chiral symmetry, yielding the three massless bosons known as pions, which are about ten times lighter than protons. This profound realization inspired about a decade before the birth of QCD by Nambu and Jona-Lasinio, laid the foundation for an effective theory description of the long-distance aspects of QCD [34], offering valuable insights into its nonperturbative aspects.

Another intriguing facet of QCD is its prediction that under certain conditions, a global center symmetry can spontaneously break, which implies that quarks and gluons could be liberated from the hadrons into a deconfined state known as quark-gluon plasma, potentially occurring at extremely high temperatures [35]. The impact of dynamical quarks and their chiral symmetry on the phase diagram of hadronic matter soon became apparent. This theoretical understanding culminated in the experimental confirmation and exploration of QGP in the heavy ion collision experiments at Brookhaven National Laboratory (BNL) and the European Organization for Nuclear Research (CERN).

In this chapter, we venture on a journey to explore one of the fascinating realms of the union of theory and experiment that has revolutionized our understanding of the strong force. We delve into the world of heavy quarkonium within the context of QGP, a mysterious state of matter that challenges our understanding of the fundamental forces shaping the universe.
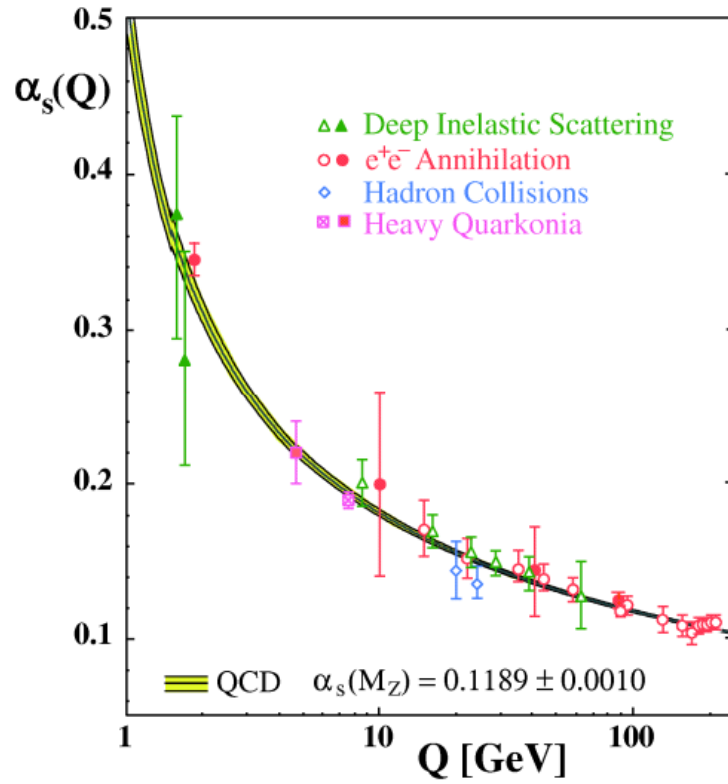
Figure 1.1: The QCD running coupling constant plotted as a function of momentum transfer. Figure taken from [36].

1.2 Heavy ion collision and quark-gluon plasma

QCD is a gauge field theory that is integral to the standard model of particle physics and is specifically used to explain the complexities of strong interaction [37]. One remarkable feature of QCD is the asymptotic freedom, which arises from the non-Abelian nature of the SU(3) group that constitutes its basis. The principle of asymptotic freedom suggests that when the momentum exchange between the quarks and gluons increases, the interactions between them become weaker (see Fig. 1.1). This means the strength of the strong interaction, quantified by the coupling constant α_s, is inherently connected to the momentum scale of the interaction. A perturbative technique (pQCD) can be used to investigate processes where α_s is small, and there are significant momentum transfers among partons [38]. This

9

method requires α_s to be expanded to higher orders [3], where the contributions from lower orders are quite significant.

Nevertheless, the perturbative framework of QCD breaks down when dealing with calculations related to low-momentum events since higher orders become apparent. This shift into a non-perturbative regime, in which the coupling constant grows, is an extremely important subject for comprehending important features of the strong interaction. Interestingly, confinement arises in this non-perturbative regime, indicating that quarks and gluons are still elusive and outside the direct observation. The only composite entities that are the subject of detection are hadrons, which are free of any net color charge. Moreover, spontaneous chiral symmetry breaking is a crucial aspect of strong interaction in the non-perturbative domain [39]. This process adds a substantial amount to the mass of hadrons, which includes protons and neutrons, among other particles. Effective Field Theories [40] and Lattice QCD [41,42] are two theoretical approaches that show promise for exploring the complexities of the non-perturbative features of strong interactions. These models provide a foundation for understanding the non-perturbative terrain of strong interactions.

Gaining insight into the characteristics of extended systems that are subjected to strong interactions offers a special way to explore the depths of strong force. Condensed matter physics examines emergent phenomena of electromagnetic interaction, such as magnetism and superconductivity. These occurrences manifest as collective behaviors rather than directly arising from microscopic interactions. The development of a many-body system with quarks and gluons at high energy density is the goal of "QCD condensed matter." Raising the temperature of the system, characterized by near-zero net baryon density, to levels exceeding 150–160 MeV ($\gtrsim 10^{12}$ K) brings about a state of plasma of quarks and gluons. In QGP, two major basic characteristics of low-temperature QCD, confinement and chiral symmetry breaking, cease to exist [43–45]. Calculations revealed that a strongly interacting system featuring zero net baryon density evolves seamlessly from a hadronic state to the

deconfined state of QGP as its temperature rises to approximately 155 MeV.

As no discontinuities are observed in thermodynamic variables, a crossover transition unfolds, allowing deconfined and confined hadronic matter to coexist, as depicted in Fig. 1.2. A substantial surge in the energy density normalized to the fourth power of temperature per the Stefan-Boltzmann law indicates the liberation of considerable new degrees of freedom around the deconfinement temperature. Interestingly, the QCD medium char-
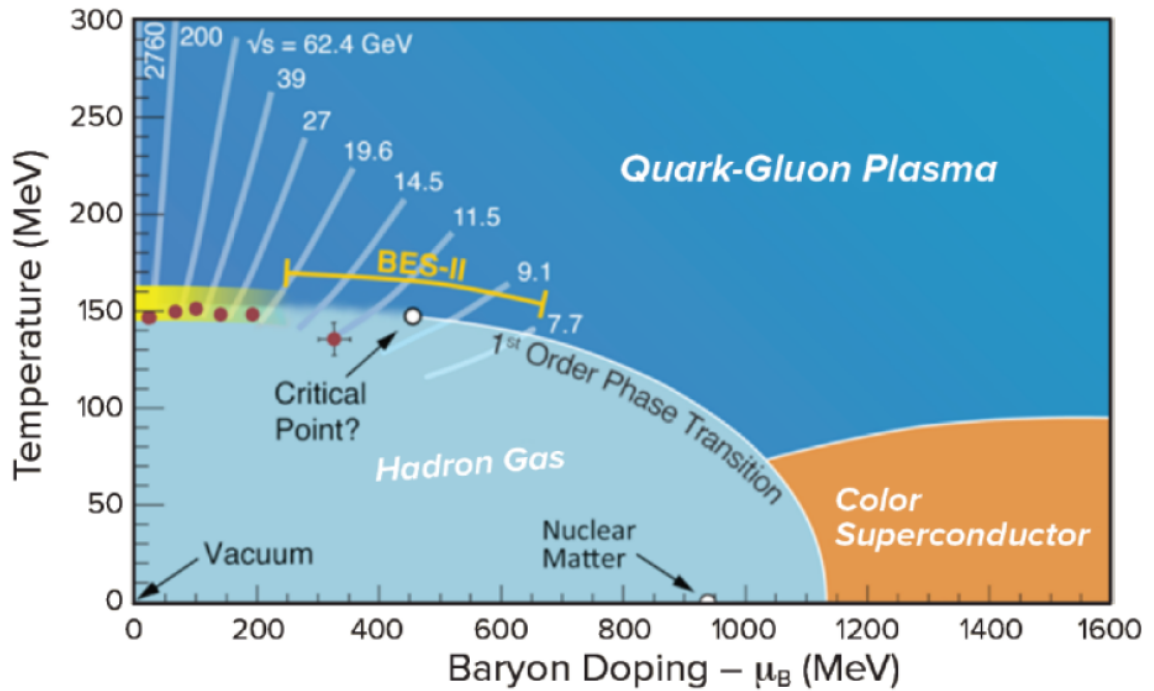
Figure 1.2: A schematic QCD phase diagram and the phases of the expanding QGP traverses in heavy ion collisions with different center of mass energy. Figure taken from [46].

acterized by zero net baryon number echoes the conditions of the early universe, where deconfined quarks and gluons subsequently hadronized around cross-over temperature T_c. A counterpart situation, marked by increased baryon density and relatively lower temperature, might also lead to the generation of the QGP. This state could potentially exist within the cores of neutron stars [47]. In laboratory settings, a condition reproducing the early universe can be replicated by colliding two heavy ions at energies in the multi-TeV range.

The Large Hadron Collider (LHC) at CERN [48] and the Relativistic Heavy Ion Collider (RHIC) at Brookhaven National Laboratory are instrumental in enabling such collisions.

1.3   Stages of heavy ion collision experiment

We create QGP in the laboratory by colliding the two heavy nuclei ultra-relativistically. This complex process can be outlined into distinct stages: (1) Initial State, characterized by universal wave functions of the colliding nuclei; (2) Large-Q^2 (the square of 4-momentum transfer) interactions of partons from the initial projectiles, setting the stage for further interactions; (3)Small-Q^2 interactions leading to pre-equilibrated parton gas; (4) thermalization and further expansion of the QGP; (5) Hadron formation as QGP cools down; (6) chemical freeze-out of hadrons where the chemical composition of particle species stabilizes; (7) kinetic freeze-out where interactions among hadrons cease away; (8) Free-Streaming of stable particles to the detector unobstructed for measurement [49]. Figure 1.3 provides a graphic representation of the details of this stage-by-stage process [50].

When heavy ions collide, they excite an extraordinarily dense parton region that deposits energy and entropy in the collision overlap zone. The impact parameter of colliding nuclei, denoting the separation between the centers of the Lorentz contracted nuclei as illustrated in Fig. 1.3, defines the overlap zone and determines the number of nucleons participating in initial inelastic interactions at least once and the total count of inelastic nucleon-nucleon collisions. When the impact parameter is minimal, the participants and collisions are high, and vice versa. The maximum value for participants is $2A$ if the colliding nuclei have an equal number of nucleons (A). Nucleons not engaged in the collision are referred to as spectators, prevailing in their path along the beam direction. A plethora of QCD processes emerge in the context of inelastic nucleon-nucleon interactions, each with a discrete spectrum of momentum transfers and a specific role.
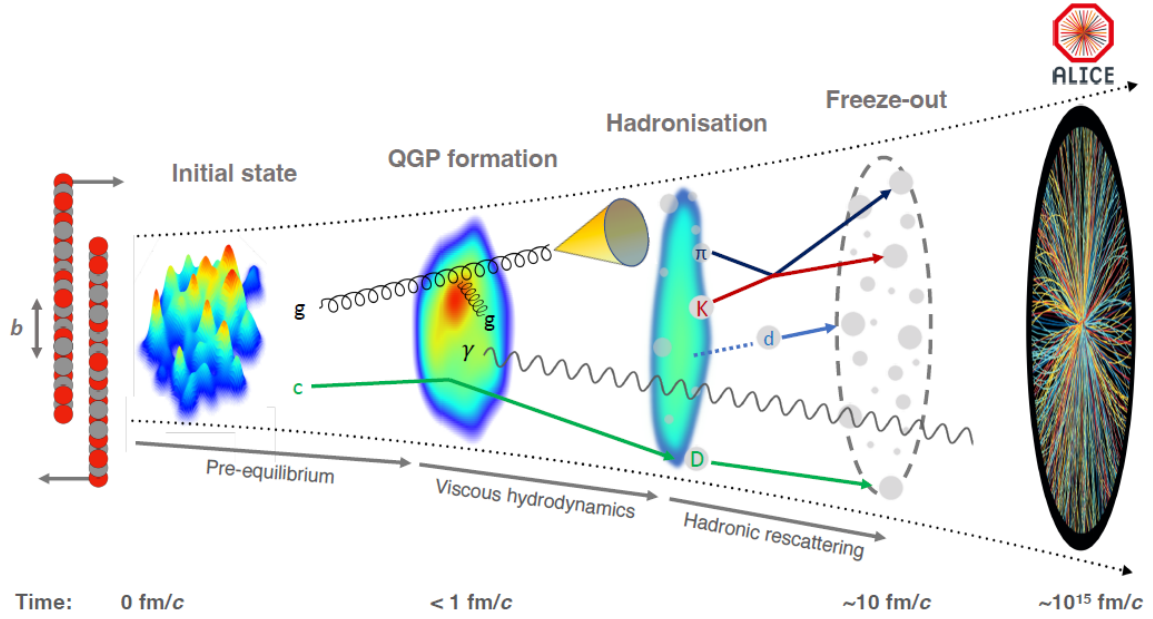
Figure 1.3: The evolution of heavy-ion collision at LHC energy. Figure taken from [50]

The smaller-Q^2 interactions take place immediately after the collision against the background of a weakly coupled pre-equilibrium stage. This, in turn, opens the door for these processes to create increasingly softer partons, which in turn helps to develop a strongly coupled QGP state. The hard processes stemming from the large-scale interactions, whose rate is determined by the number of initial hard collisions, play a major role in generating high-momentum gluons and heavy quarks. The heavy quarks generated in hard processes can combine to form quarkonia, which are the bound states of heavy quarks and antiquarks. Nevertheless, the production rate of quarkonia is suppressed due to the screening of the binding force between the quark and antiquark by the presence of the color charge of quarks and gluons of the QGP medium. This suppression exhibits a close relationship with the temperature of the QGP.

Investigating QGP evolution in processes dominated by soft interactions beyond 1 fm/c yields fascinating findings. The QGP constituents are strongly coupled, and the mean free

path is expected to be significantly smaller than the size of the QGP fireball. Consequently, numerous interactions drive the expansion of the QGP. This expansion is largely affected by the non-uniform distribution of energy density within the initial state across spatial dimensions, which results in a pressure gradient within the early stage of the QGP. The length scales of these gradients exceed the mean free path, and the subsequent evolution exhibits characteristics that are described by the principles of hydrodynamics. The hydrodynamic expansion of QGP demonstrates a radial pattern as a consequence of higher pressure at the center of the QGP compared to the periphery. The speed of this hydrodynamic expansion is mainly influenced by the bulk viscosity of the QGP liquid drop, reflecting its resistance to changes in volume. An anisotropic flow emerges as a consequence of directional-dependent pressure gradients due to spatial anisotropies present in the initial state originating from the noncentral collision of nuclei when the impact parameter is nonzero. These spatial anisotropies transform into momentum anisotropies through the hydrodynamic response. This transformation process is governed by the shear viscosity of the QGP, a quantity that resists the deformation in the fluid context.

Due to the nuclei's positive charge, the motion of the incoming beams induces a large magnetic field. This magnetic field arises from the protons within the colliding nuclei, which are moving with relativistic energies. While for central collisions, the magnetic fields cancel out, for non-central collisions with finite impact parameters, the net magnetic field can be very large, which can be of the order of QCD scale. This magnetic field can exert a huge influence on the trajectory of quarks during the QGP phase. The chiral Magnetic Effect (CME) is one interesting phenomenon that appears within this magnetic environment. The CME is believed to result from strong parity violations locally and splits positively charged and negatively charged quarks in the QGP. The electrically charged quarks can be moved according to the electric field induced by the decaying magnetic field. According to Lenz's law, this effect prolongs the magnetic field decay. The high-temperature QGP also generates

14

thermal radiation, which follows a distinctive behavior in the QGP as it doesn't interact via the strong force. This offers a valuable way to gain information regarding the temperature at early to the later stages of QGP. Furthermore, there is a tendency towards the production of strange quarks in the QGP stage. These quarks have masses less than the temperature of the QGP and, therefore, below the deconfinement temperature. This enhancement of strange quark production highlights the complexity of phenomena observed in this exotic state of matter.

The hadronization process starts occurring in the regions of the QGP that gradually cool below the critical transition temperature as the QGP expands. Since the temperature and energy density of this medium are expected to decrease with the increase in distance from the collision center, and lattice QCD insights suggest that the transition from the QGP to hadrons occurs as a smooth cross-over, the hadronization process happens at different times and different places of the phase-space. The extremely energetic components of a jet, known as hard partons, will travel along a path of hadronization and fragmentation similar to that of elementary collisions. The patrons at lower momenta can combine into hadrons via coalescence if they share space and momenta like other partons. The recombination of heavy quarks with their corresponding heavy antiquarks is also supported by this complex fabric of interactions within the QGP. Quarkonia is created as a result of this fusion, providing a further route for producing closed heavy hadrons. This supplementary mechanism is a counterbalance to the quarkonium suppression in the QGP.

A variety of particles are produced, including protons, kaons, and pions, as a result of the hadronization process. Here, the energy density of the hadron gas reaches a level that allows for inelastic collisions among the particles, which in turn would drive a change in the chemical compositions of different particle species. In particular, the loosely bound deuterons are subjected to these interactions, as their formation or dissolution can readily take place. Such interactions continue until the chemical freeze-out temperature is reached;

at that point, the composition of particles is finally fixed. Elastic collisions persist beyond this stage and only terminate when the kinetic freeze-out temperature is achieved, generally happening at 10 fm/c. Beyond this stage, the momenta of particles are fixed and traveled toward the detectors to undergo detailed measurement.

1.4   Signatures of quark-gluon plasma

A variety of experimental approaches are utilized to investigate each phase of heavy-ion collisions, spanning the initial state, the QGP phase, and the hadronic phase. These probes demonstrate varying degrees of sensitivity to the distinct phases. A fundamental parameter crucial to many of these probes is the Lorentz-invariant differential yield of final state particles, which is defined as:

$$E\frac{d^3N}{dp^3} = \frac{1}{2\pi p_T}\frac{d^2N}{dp_T dy},$$

(1.1)

the number density of the particle momentum scaled by the energy (E). This will depend upon the transverse momentum, p_T, and rapidity, y, of the measured particle species under consideration. Pseudorapidity ($\eta = -\ln\tan(\theta/2)$, θ is the polar angle of the particle with respect to the beam axis) is employed in instances where the particle species is unknown, and both are interchangeable when the particle energy significantly exceeds its mass. This section will discuss only the probes to the QGP phase, not the initial state and hadronic phase.

The formation of hot and dense nuclear matter occurs within an incredibly small region of space, and it persists for a very short period, measuring just a few femtometers and lasting for about ten femtoseconds due to the fast expansion and cooling. At the detector end, the observations are restricted to the energies, momenta, and azimuthal dependences of colorless particles, such as hadrons, leptons, and photons, which emerge when the nuclear matter has transitioned into a relatively cold and non-interacting gas. This situation may also

manifest when excited nuclear matter is created instead of the QGP. Therefore, to validate the creation of the QGP in heavy ion collision and analyze its thermodynamic and transport properties, we rely solely on the observed signatures.

For precise observations, it is crucial to distinguish the medium effects from the other stages of evolution. Based on the temperature, which is a pivotal parameter influencing the medium expansion, observables can be classified into two groups: those associated with low temperatures, referred to as soft probes, and those related to high temperatures, known as hard probes. Soft probes are employed to describe collective behaviors and thermodynamic properties, such as the average temperature of the medium, as they are produced throughout the QGP evolution. These observables include low transverse momentum hadrons, thermal photons, di-leptons, etc. In contrast, hard probes consist of high-momentum particles produced in the early stages of the collisions, like heavy quarks and quarkonia. They act as independent degrees of freedom while traversing the created medium. A key observable related to hard probes is the suppression of quarkonia, which offers insights into the medium temperature and color screening. Among the various indirect probes, the most powerful ones include collective flow, jet quenching, and quarkonia dissociation. The observations of these events in heavy-ion collision experiments at RHIC and LHC have explained the near-perfect fluid and strongly coupled nature of the QGP.

1.4.1 Anisotropic flow

An experimental evidence for creating QGP in heavy-ion collision experiments is the anisotropic emission patterns of charged particles within the plane transverse to the beam direction. The non-central collisions of the Lorentz contracted nuclei create an almond-shaped overlap region. Consequently, immediately after the collision, the initial state exhibits spatial anisotropy. The initial momenta of the newly created particles are predominantly oriented in the longitudinal direction, with transverse momenta distributed isotropically. The final

distribution stays isotropic if there is no interaction between these particles. On the other hand, local thermal equilibrium is probably reached when interactions take place, allowing the system to be represented in terms of thermodynamic parameters such as temperature and pressure. In such instances, the spatial anisotropy of the initial state causes an anisotropic pressure gradient in the transverse plane due to these interactions and collisions of the medium particles. Consequently, the medium undergoes evolution, resulting in a momentum anisotropy in the final state as it approaches equilibrium [51, 52].

Over the past two decades of heavy ion collision history, the anisotropic flow has been observed by numerous experimental collaborations at facilities such as the Alternating Gradient Synchrotron (AGS), Super Proton Synchrotron (SPS), RHIC, and, more recently, at the LHC [53]. The collective flow phenomenon can be analyzed by expressing the observed particle spectrum measured in the Fourier series, allowing researchers to extract valuable insights into the features of the medium and its evolution,

$$E\frac{d^3N}{d^3p} = \frac{1}{2\pi}\frac{d^2N}{p_T dp_T dy}\left(1 + \sum_{n=1}^{\infty} 2v_n \cos\left(n\left(\phi - \psi_R\right)\right)\right),\qquad(1.2)$$

where ϕ is the azimuthal angle of an out going particle and ψ_R is the reaction plane angle. The Fourier coefficients v_n describe the various flow modes and can be measured as

$$v_n = \langle\cos(n\phi)\rangle.\qquad(1.3)$$

For example, v_1 corresponds to directed flow, v_2 gives elliptic flow, v_3 refers to triangular flow, and so forth. Hence, researchers have extensively analyzed the implications of momentum anisotropy, often referred to as elliptic flow, using a variety of methods. Elliptic flow of different particle species in Pb–Pb collisions at $\sqrt{s_{NN}} = 5.02\ TeV$ for different centrality classes in comparison to various models are shown in Fig 1.4. It is essential to mention that this momentum anisotropy is present at every stage of the space-time evolution, gradually developing non-zero values as soon as the space-time evolution begins,

predominantly within the hydrodynamical region [51, 52]. Moreover, it has been discovered that the QGP displays an exceptionally small shear viscosity (η) to entropy density (s) ratio, which may be among the smallest ratios in all of the known fluids in nature. A wide range of theoretical studies, from kinetic theory to holographic theory, corroborate this fascinating discovery [54, 55].
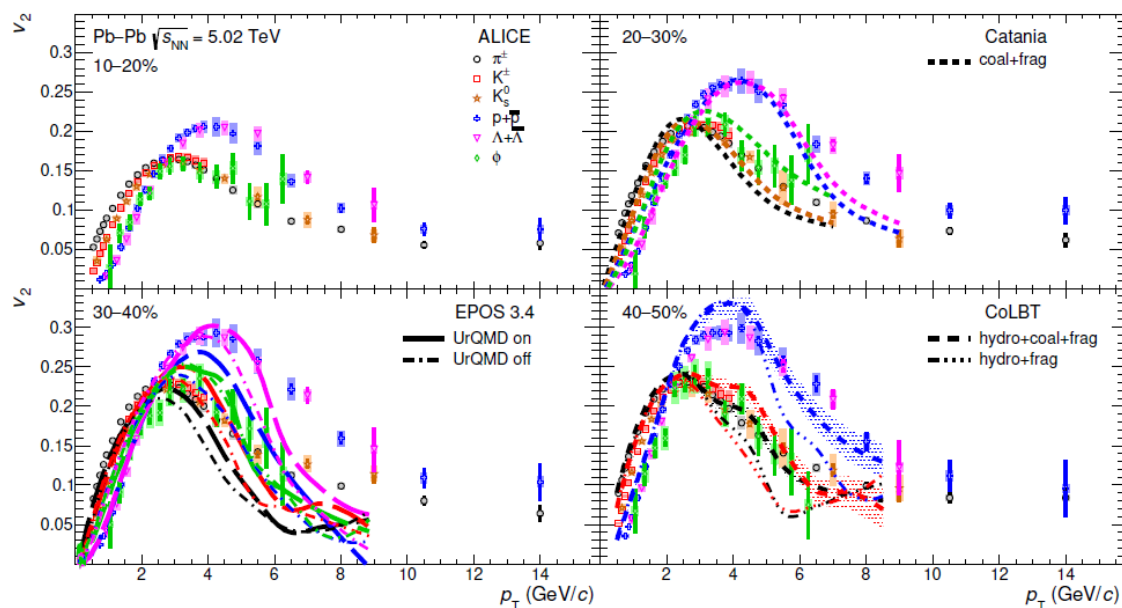
Figure 1.4: p_T-differential v_2 for different species of particles in Pb–Pb collisions at $\sqrt{s_{NN}} = 5.02\ TeV$ for various centrality classes in comparison to the EPOS 3.4 [54], Catania [56], and CoLBT [57] models. Figure taken from [50]

1.4.2 Jet quenching

When a scattered parton possesses a transverse momentum greater than a few GeV/c, it ventures on an independent evolutionary trajectory, starting the journey before the first femtosecond of heavy ion collision. With a substantial spatial extent and lifespan of 10 femtoseconds, QGP serves as the environment through which this high-energy parton traverses. It generates a jet shower that simultaneously goes through its own dynamic evolu-

tion and passes through the rapidly cooling and expanding QGP. During this process, the color-charged constituents of the jet shower interact with the medium color-charged constituents, leading to modifications in the shower itself [58, 59]. These modifications, called "jet quenching," provide a singular and profound insight into the structure and dynamics of the QGP since they are both theoretically calculable and physically observable. From an experimental perspective, there are a few unique manifestations that indicate jet quenching:

- Energy loss measured through inclusive yield suppression: medium-induced energy transport to huge angles to the jet direction;

- Medium-induced modification of jet constituents distribution, observed via the radial energy profile, fragmentation functions, and jet substructure;

- Jet centroid deflection caused by the soft multiple scattering within the QGP observed as medium-induced acoplanarity of coincidence measurements.

As it provides a consistent and thorough understanding of this phenomenon, this multimodal method of evaluating jet quenching offers an invaluable opportunity. The contribution it makes to our comprehension of the fundamental mechanisms of jet quenching in the QGP is substantial. Interactions between high-energy partons and the QGP can be broadly categorized into elastic interactions involving the propagating parton and the constituents of the medium. Additionally, there are inelastic interactions characterized by medium-induced gluon radiation events. The latter processes occur concurrently with the spontaneous splittings of the parton shower, a phenomenon also observed in proton-proton (pp) and other elementary collisions, even in the absence of the QGP, commonly referred to as vacuum emissions. The radiative processes are the predominant energy loss mechanism at high p_T. This has been analyzed [60, 61], and the results show that interference of scattering and emission processes cause a distinctive energy loss dependence on the in-medium path length. These

studies generally arrive at the conclusion that radiative energy loss predominates over collisional energy loss, which means that the amount of energy lost by a fast-moving jet does not depend linearly on the path traversed through the QGP medium [62]. Furthermore, the experiment shows that the heavy quarks with radiative energy loss is strongly dragged in the QGP medium [63].

1.4.3 Dileptons and Photons production in QGP

The quarks and anti-quarks interact in QGP to form virtual photons γ^*, which subsequently decay into dilepton pairs (leptons l^- and anti-leptons l^+). The Drell-Yan process is the most common mechanism of dilepton production in QGP:

$$q + \bar{q} \rightarrow \gamma^* \rightarrow l^+ + l^-. \tag{1.4}$$

The created leptons and anti-leptons pass through the collision region. Given that the lepton-quark interaction is electromagnetic in QGP and the cross-section $\sim (\alpha/\sqrt{s})^2$ (where $\alpha = 1/137$ is the fine-structure constant, and $\sqrt{s}$ is the lepton center-of-mass energy) is much smaller than the strong interaction cross-section. Leptons are, therefore, unlikely to interact with the QGP after creation and to get at the detector directly. We can determine whether a QGP state has been achieved by examining the lepton pairs, which also convey information about the thermodynamic properties of the medium at the time of their generation. The other probes of the early collision stage are real or virtual direct photons, which materialize a lepton-antilepton (l^+l^-). In the QGP, they are also generated by quark-antiquark interaction:

$$q + \bar{q} \rightarrow \gamma + g. \tag{1.5}$$

This is known as the annihilation process. The analogous electromagnetic processes $q\bar{q} \rightarrow \gamma\gamma$ is permitted, but it has a very smaller cross-section compared to $q\bar{q} \rightarrow \gamma g$ by a factor α_e/α_s. Because photons do not further interact with the QGP once they are pro-

duced, photon analysis provides exactly the same information as dilepton. Their production cross-section is exceedingly modest since it is proportional to the square of the fine structure constant. Their mean free path, even in an extremely dense QGP, is approximately 50,000 fm, which is far larger than any heavy-ion fireball, as their interaction cross-section is negligible. They convey pristine information about the momentum distributions of their parent quarks and antiquarks into the detector and exit the collision zone without any further interaction, in contrast to all other hadronic probes. Real and virtual photons are emitted throughout the evolution of heavy ion collision, and their measured spectrum thus integrates over the expansion history of the QGP fireball. Unfortunately, a huge background of indirect photons and a significant background of uncorrelated lepton pairs originating from electromagnetic and weak decays of hadrons after hadronic freeze-out cause noise problems for the directly emitted photons and dileptons. This makes determining the proper physics from the measurement of these pure electromagnetic signals challenging [64–66].

1.4.4 Strangeness enhancement

One of the first signals proposed for the QGP formation is an enhanced strangeness production in heavy-ion collisions relative to pp collisions [67–70]. This establishes a connection between the hadronic and partonic phases as well. Due to the large mass of the strange quark ($m_s \simeq 170\text{MeV}$) compared to up and down quarks, the production of particles containing strange quarks is typically suppressed in hadronic processes. The dominant production mechanism of $s\bar{s}$ pairs involves gluons only when the matter becomes QGP. The temperature in QGP is of the order of strange quark mass, and the production of $s\bar{s}$ pairs in interactions of two gluons ($gg \rightarrow s\bar{s}$) should be favored by the quick filling of the phase space available for up and down quarks. Strange quarks are created in pair-production processes. Unlike the up and down quarks, they are produced in collisions between constituents of the plasma. Therefore, the $s\bar{s}$ pairs production is enhanced in the presence of QGP.

A few of the strangeness possessing baryons are $\Lambda(uds)$, $\Xi(qss)$ and $\Omega(sss)$ etc. Some collaborations WA97 [71] and NA49 [72] have clearly established the relative enhancement of (anti-)hyperon yields (Λ, Ξ and Ω) in Pb-Pb collisions compared to p-Pb collisions. NA49 collaboration has observed a prominent and sharp maximum in the excitation function of K^+/π^+ ratio at 30A GeV [73]. This sharp maximum is referred to as "horn", which is not seen in p+p collisions. As the predominant carrier of anti-strangeness at SPS energy, K^+ serves as a reliable indicator of the overall strangeness production in the collision. The strangeness to entropy ratio is expressed as K^+/π^+. The statistical model predicted a dramatic increase in this quantity, suggesting the early stage as a result of the transition to a deconfined state. Ξ^- and Λ' are examples of other strange particles for which the same collaboration has also observed a similar maximum at the same beam energy. The NA49 group's investigation into the excitation function of strangeness production has rekindled a thought-provoking discourse regarding the significance of strangeness as a signature for the deconfinement phase. The analysis of the strangeness enhancement in heavy-ion collisions is significantly enriched by complementary lattice investigations.

1.4.5 Quarkonium suppression

The bound states of a $c\bar{c}$ pair (charmonium) or $b\bar{b}$ pair (bottomonium), known as heavy quarkonia, have been the focus of much research since their discovery in the 1970s. While much progress has been made, a full understanding of their characteristics has to be attained. Within the framework of QCD, the examination of their creation processes, the rich spectroscopy of the many states, their decay modes, etc, is still a vibrant research area [74]. Additionally, quarkonium states are indispensable for understanding the QGP and its characteristics. It was discovered early on that immersing quarkonia in a deconfined medium could have varying effects on the binding of the heavy-quark pair. The QCD force is screened by the large density of free color charges in the QGP, which finally causes the

quarkonium to dissolve [75]. A large number of theoretical and experimental research have been inspired by this straightforward yet profound principle, and they have shown novel and occasionally unexpected consequences. It was the goal of early research to directly relate the temperature of the deconfined phase to the suppression of the quarkonium states [76].

The intricate spectroscopic structure of quarkonia, where binding energies range from a few MeV ($\psi(2S)$) to more than 1 GeV ($\Upsilon(1S)$), could result in a "sequential suppression" as temperature rises, where the weakly bound states melt at near transition temperature T_c, and the more tightly bound states survive up to a dissociation temperature $\sim 2T_c$. In nuclear collisions, the temperature of the QGP can, in principle, be manipulated by adjusting the centrality of the collision or its center-of-mass energy. Quarkonium could serve as an ideal thermometer for the medium if theoretical investigations could precisely determine the melting temperature for each state. The above views hold true when considering a static picture of the medium in which the quarkonium states are submerged. Several effects contribute to a more complex depiction when studying the dynamics of the bound states and their interaction with an expanding medium. It is specifically a multi-stage process that forms the quarkonium states [40] (creation of the $q\bar{q}$ pairs and forming their bound states) that extends across a period of time encompassing a substantial portion of the collision history.

Moreover, the imaginary part of the quarkonium potential, computed at $T > 0$ in effective field theories, corresponds to the collisional damping of the states. This leads to a loss of correlation in the pair and induces in-medium changes in the spectral functions [77]. Moreover, in a system with a high heavy quark multiplicity, the recombination of previously destroyed ones or the combination of uncorrelated pairs from various hard scattering processes can result in a large increase of the quarkonium yields [78], counteracting the suppression. Quarkonia generated through the recombination process can acquire collective flow effects if there is a partial or complete kinetic equilibrium among the deconfined

heavy quarks within the medium [79]. Lastly, quarkonium-meson breakup effects may also affect the yields during the hadronic stage of the collisions; these effects may be especially significant for weakly bound states [80,81]. Quarkonium generation in the hot QCD medium is treated theoretically in a variety of ways, including statistical hadronization, transport models, hydrodynamics, and the more modern technique of quantum dynamics.

A more detailed description of quarkonia, especially in the potential model formalism, will be presented in the next chapter.

1.5 Magnetic field in heavy ion collision

Heavy-ion collision experiments offer a sound environment to study hot nuclear matter in the magnetic field. Heavy-ion collisions are expected to produce an intense electromagnetic field due to the oppositely moving ultra-relativistic protons, especially in the early stages of the collision. The estimated peak value of the magnetic field strength for the Pb+Pb collision is $eB = 15m_\pi^2 = 1.5 \times 10^{19}$Gauss at the LHC energies [82] (The LHC produces a magnetic field that is ten times greater than the RHIC). The ALICE collaboration studied the directed flow of D/D^0 mesons and charged hadrons to probe the presence of this immensely powerful magnetic field. Intriguing evidence of the presence of a strong magnetic field in the heavy-ion collisions is provided by these LHC results in conjunction with the RHIC observations [83]. The heavy-ion collision experiments produce magnetic fields that are among the strongest known in the current universe, bigger than those produced by neutron stars. In addition to gold, the RHIC has conducted collision tests with heavy nuclei such as Cu+Au and U+U. The electromagnetic field generated in these systems has been studied in Refs. [84–88].

Due to the larger charge and size of the Au nucleus compared to the Cu nucleus, the collisions involving Cu+Au exhibit geometric asymmetry. This may generate a finite elec-

tric field in addition to the magnetic field at the order of m_π^2 in the reaction plane Au-to-Cu direction [87]. However, the magnitude of the magnetic fields is in the same order as that of Au+Au collisions. This has been observed that the event-averaged strength of the magnetic field in the U+U collisions at $\sqrt{s}_{NN} = 193$ GeV is less than in Au+Au collisions at $\sqrt{s}_{NN} = 200$ GeV [88]. The electrically charged heavy nuclei cause an electric current while moving at relativistically high velocity $v_z = \sqrt{1 - \left(2m_N/\sqrt{s_{NN}}\right)^2}$ along the beam direction (z- axis) (m_N is the nucleon mass) at a non-zero impact factor b which in turn generate the magnetic field. The magnetic field produced in the heavy-ion collision can approximately be estimated employing the Biot-Savart law and take the following form,

$$-q_f B_y = 2Z_N \gamma \frac{q_f^2}{4\pi} v_z \frac{4}{b^2}, \tag{1.6}$$

where $\gamma^{-1} = \sqrt{1 - v_z^2}$ is the Lorentz factor and Z_N is the atomic number of the heavy nuclei. The magnetic field is pointed perpendicular to the reaction plane. The expression of the magnetic field from the Biot-Savart law is very primal. Better estimations of the magnetic field have been done by combining the knowledge of nucleon distribution function in the nuclei [89, 90]. Such studies used the Liénard-Wiechert formula to estimate the electromagnetic fields.

Advanced transport models have been used to study various aspects of electromagnetic fields in a heavy-ion collision, including the correlation between matter geometry and the fields, the event-by-event fluctuations of the fields, and the dependence of the impact factor and collision energy on the generated electromagnetic fields [91, 92]. The life span of the magnetic field in the medium is still unknown despite recent advances in measuring the field strength. As of this point, there is no adequate theory or model to explain how the magnetic field evolves during heavy-ion collisions. Analyses showed that the electrical conductivity σ of the QGP medium strongly affects the decay time of the magnetic field in the medium [93, 94]. This can be comprehended from Faraday's law of electromagnetic induction. The

decay of a magnetic field induces an electric current in the plasma, subsequently generating a new magnetic field. The time evolution of the magnetic field in the static QGP can be expressed as,

$$\frac{\partial \vec{B}}{\partial t} = \frac{1}{\sigma} \left(\nabla^2 \vec{B} - \frac{\partial^2 \vec{B}}{\partial t^2} + \vec{\nabla} \times \vec{J}_{\text{ext}} \right),$$

(1.7)

where $\vec{J}_{\text{ext}}$ is the external current due to the movement of protons. According to the equation, the magnetic field decays much more slowly in a highly conducting medium than it does in a vacuum. The majority of investigations on the characteristics of magnetized QGP assumed a constant magnetic field. The charged fermions move in a cyclotron fashion due to the steady homogeneous magnetic field. The inverse Larmor radius quantifies the curvature of the charged particle in the magnetic field. It is necessary to take into account the Landau quantization of the cyclotron motion when the magnetic field is high enough. This suggests that the thermal energy particles are substantially smaller than the cyclotron frequency.

Chapter 2

Quarkonia in quark gluon plasma

The QGP medium created in heavy-ion collision (HIC) experiments exhibit a remarkably small size (~ 10 fm) and an extremely brief duration ($\sim 10^{-23}$ sec) [95–98]. The transient nature of this medium limits the feasibility of exploring its properties quantitatively using external probes. Consequently, reliance is primarily placed on internal probes to scrutinize the created matter. In this context, heavy quarks (charm and bottom) and their bound states, namely heavy quarkonia, hold significant importance [99–102]. Due to their elevated masses, these particles are predominantly produced at the early stages following collisions and behave almost as independent degrees of freedom throughout the various phases of the created matter. However, they are minimally affected by the QGP medium as they pass through it, resulting in distinctive signatures observed in their final yields at detectors. In the seminal work by Matsui and Satz [75], it was suggested that the production of heavy quarkonia would be suppressed in high-energy heavy-ion collisions due to the Debye screening provided by the plasma, reducing the effective interaction between constituent particles. This suppression phenomenon has since become a central focus for researchers aiming to unravel the complex interplay between heavy quarkonia and the QGP, driving advancements in both theoretical frameworks and experimental methodologies.

2.1   Quarkonium bound states

The bound states of heavy quarks and their antiquarks are known as heavy quarkonia. The discovery of the J/ψ meson, whose mass is around 3.1 GeV, was the first indication of the

existence of heavy quarks. J/ψ is the bound state of a charm quark (c) and its antiquark ($\bar{c}$), where the masses of these quarks are estimated to be 1.27 GeV. Charmonium is the common term for the $c\bar{c}$ bound state. Nearly simultaneously, J/ψ was found at Stanford Linear Accelerator Center and at Brookhaven National Laboratory in 1974. The next mass level up is represented by the Υ meson, which has a mass of roughly 9.5 GeV and is composed of a bottom quark-antiquark pair ($b\bar{b}$), which has a mass of 4.18 GeV. Bottomonium state is the common terminology for the $b\bar{b}$ bound state. Charmonium and bottomonium resonance states have extended lifetimes because of their incredibly small widths. Because of this, after they are formed in the collision, they would not start to decay until they have left the collision zone. Nevertheless, the open charm mesons, $D(c\bar{u})$, and beauty mesons, ($B(b\bar{u})$, can also result from the binding of charm and bottom quarks with light quarks. In comparison to the normal hadrons, the binding energies of $c\bar{c}$ and $b\bar{b}$ ground states are significantly larger, and their sizes are much smaller than the typical hadronic scale $\Lambda \sim 0.2$ GeV. Additionally, a variety of stable bound states with various quantum numbers other than the low-lying ground states of charmonium and bottomonium can be possible. The excited states are larger than the ground state and less tightly bound.

The quarkonium masses are primarily caused by the heavy charm and bottom quark masses, whereas the masses of light hadrons are typically produced by the interaction between the nearly massless quark constituents. This allows the non-relativistic potential model to compute the quarkonium state properties. The separation between hadrons becomes smaller than their individual sizes as the energy density of matter increases. At this point, their wave functions begin to overlap and form the deconfined medium of quarks and gluons. Lattice studies confirm that heavy quarkonia can even survive in the deconfined medium since their size is of the same order as parton separation in the deconfined state. Once such a medium is created in an ultrarelativistic nucleus-nucleus collision, it expands, cools, and harmonizes after crossing the confining point. Understanding the properties of

the quarkonia in the deconfined medium using potential model formalism is the central idea of this thesis.

2.1.1 Debye screening

The electric field inside a perfect conductor is zero, as is known from the classical picture of electromagnetic theory. Conductors have an accumulation of free electrons. The charge will move to its surface if an external electric field is applied to cancel the electric field inside the conductor. Also, a test charge placed inside a conductor will find its way to the surface. The electric field is screened in a way. The screening prevents the electric field lines of force from penetrating and entering the conductor. For an insulator, this phenomenon is obviously not going to occur. When enough thermal energy is present, the intermolecular bonds are broken, allowing molecules to move freely and become a gaseous state. We can ionize the gas to have freely moving ions and electrons by increasing the temperature even further. This state of matter is new because it differs from previous states in a few intriguing ways. Previously suppressed degrees of freedom are introduced into the play during this phase. Matter conducts electricity and is not electrically neutral when it is in the plasma state.

Placing a test charge in the medium causes a fascinating phenomenon. The thermalized medium alters the electric field that was created as a result of the test charge. The potential now shifts from being Coulombic to Yukawa. As a result, a new scale that describes the electric field shielding surrounding the test charge emerges. This new quantity characterizing plasma is referred to as Debye screening length. Anywhere beyond the Debye radius, the electric field falls exponentially to zero. The electric field is now contained inside the sphere of influence by the Debye screening. The electric field appears as follows for a test charge Q in the medium,

$$V(r) = -\frac{Q}{4\pi\epsilon_0 r}e^{-r/r_D},\tag{2.1}$$

where r_D is the Debye radius, which describes the plasma screening. The influence of the test charge is limited approximately within the Debye sphere. Imagine now an electric dipole with a length greater than the Debye radius. It will dissociate into free charges and cease to be a dipole, becoming a part of the medium instead.

When there are three distinct colors and randomly moving color charges, one could also anticipate a similar effect in QGP. We shall now investigate a color dipole in a deconfined medium instead of an electric dipole. They are tightly bound in a colorless environment or a vacuum. The nonrelativistic potential, which will be presented shortly, can characterize the bound state of such a heavy quark anti-quark pair. The prime motive is now to study those bound states in QGP. The potential is modified by the plasma in a very similar manner to electromagnetic plasma. This effective potential permits us to overlook the medium by considering the influence of the medium in the modified potential. Additionally, bound states of heavy quarkonia in the medium are provided by this potential. Clearly, none of the bound states will be larger than the Debye sphere. Hence, those vacuum-bound states with sizes greater than r_D cannot exist in the medium. They are not present in the medium and cannot be produced as long as the temperature stays unchanged. The missing bound states can predict both the temperature of the plasma and the creation of QGP. H. Satz and T. Masui originally suggested the concept of using suppression of quarkonia as a probe in static plasma [75], and it is still one of the most important recommendations for comprehending the medium.

The Debye radius can be decreased by raising the temperature. As a result, shorter and shorter color dipoles might melt in the medium as the temperature rises. In essence, a QGP thermometer is introduced by this sequential melting [103]. One can forecast the medium temperature just by understanding which states are melted. Considerable research has been done on the sequential suppression pattern for various charmonium [104] and bottomonium [105] states. In the context of lattice QCD and a number of phenomenological

31

models, the threshold temperature for various states is computed. To determine the dissociation temperature for various quark-antiquark bound states, more meticulous and accurate calculations in lattice and other branches can be used to research quarkonium states in the deconfined medium.
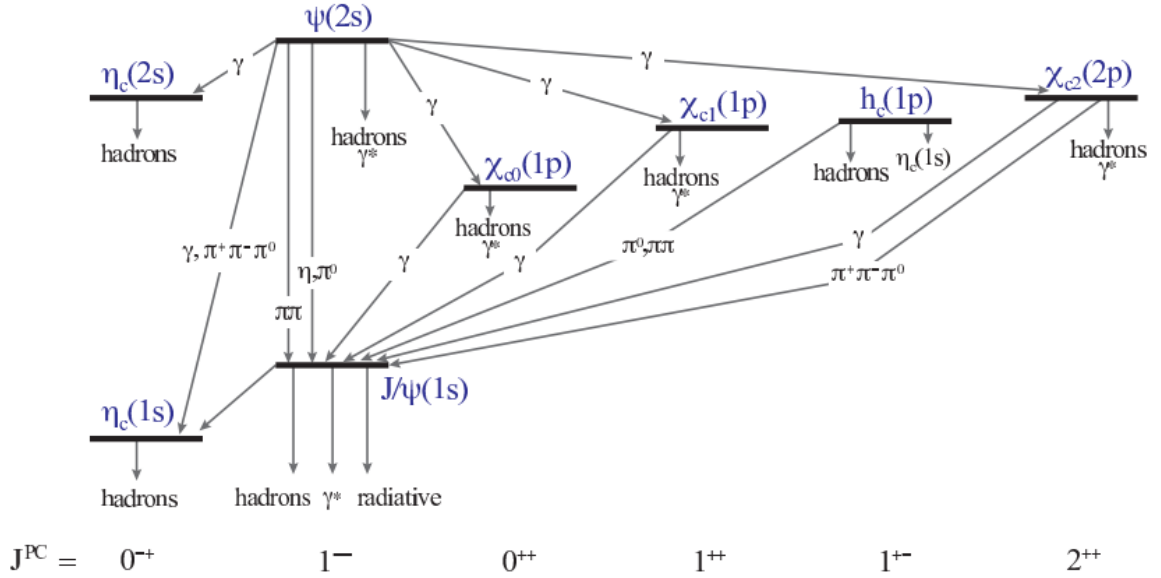
Figure 2.1: An illustration of the charmonium spectrum along with the decay channels of each state [106]. Figure taken from [107]

2.2 The Potential model

Given the significantly larger mass of heavy quarks compared to the QCD scale, the non-relativistic potential model proves to be a valuable tool for investigating the bound states of quarkonium. This model offers a reliable framework for understanding quarkonium spectroscopy (see Fig. 2.1). The Cornell potential [108, 109] can be used to define the potential for a $Q\bar{Q}$ pair at separation distance r in vacuum ($T = 0$),

$$V(r) = -\frac{\alpha}{r} + \sigma r. \tag{2.2}$$

The coupling strength α and the strong coupling constant α_s are related, *i.e.,* $\alpha = \frac{4}{3}\alpha_s$, and the confining strength is denoted by the string tension $\sigma = 0.18$ GeV^2. The Cornell potential, a composite of the Coulomb and linear potentials, plays a pivotal role by effectively incorporating two fundamental features of Quantum Chromodynamics (QCD): asymptotic freedom (at high energy or short distance) and quark confinement (at low energy or large distance) [110]. Its significance extends to various aspects of heavy quarkonia studies, encompassing the exploration of the transition between confined and deconfined phases of matter [111] and the computation of masses for diverse heavy quarkonium states.

The application of potential models to study quarkonia states at finite temperatures was first introduced by the authors in Ref. [112]. Subsequently, quarkonium spectral functions and meson current correlators have been derived from potential models [113–120] and compared with first-principle lattice QCD calculations [121–123]. Additionally, the imaginary part of the potential, arising from the interaction with the medium, contributes to the thermal dissociation width of quarkonia states [77, 124]. The dissociation of quarkonia in an anisotropic QCD medium has been explored by the authors in Ref. [125, 126]. Analyses on the velocity dependence of screening properties have been conducted in several works [127–131]. The medium-modified potential of a static quarkonium in a moving thermal bath and its velocity dependence was investigated in Refs. [133], considering the orientation of the quark-antiquark pair with respect to the direction of the medium velocity. The solution of the Schrödinger equation provides insights into the characteristics of quarkonium-bound states, analogous to the positronium system.

2.2.1 Quarkonium potential at finite temperature

Lattice QCD and potential model studies are the two methods used to ascertain the in-medium properties of the various quarkonium states quantitatively. In finite temperature lattice QCD, the quarkonium spectrum can be directly determined by building the Euclidean

correlators for a given quarkonium state. Advancements in effective field theories (EFT) have led to a better knowledge of integrating the successive scales associated with the heavy quark-bound states to create prospective models, such as NRQCD, pNRQCD, etc. Relativistic effects have very little effect on these states because the relative velocities of the heavy quarks in each quarkonium are sufficiently less. For charmonia (bottomonia), for instance, the relative speed is around 0.3 (0.1) times the speed of light in the rest frame of the respective quarkonia. Potential models were first used to calculate the masses and radii of quarkonia states. The potential includes confinement in the long range, which can be calculated using lattice simulations, and coincides with the Coulomb potential at short distances, which can be estimated using perturbative QCD.

The screening in the form obtained in one-dimensional QED, a classic work by Karsch, Mehr, and Satz (KMS), served as the foundation for the first quantitative studies of quarkonia at finite temperature [112]. Debye screening causes the potential to be screened when quarkonia are immersed in a medium at a temperature T. At finite temperature T and separation distance r, the screened Cornell potential can be expressed as follows,

$$V^{KMS}(r, T) = -\frac{\alpha}{r} e^{-m_D r} + \sigma r \left(\frac{1 - e^{-m_D r}}{m_D r} \right), \tag{2.3}$$

where $m_D(T)$ is the Debye screening mass, the inverse of the Debye radius. Upon utilizing these inputs to solve the Schrödinger equation, it was shown that although J/ψ remained stable until around $1.2\ T_c$, both ψ' and χ_c fundamentally dissociate at $T = T_c$, where T_c is the deconfinement temperature. Due to Debye screening, this method is highly effective at estimating the dissociation temperatures of quarkonia, yet it has some drawbacks. For example, the second term in the screened potential corresponds to the σr screening, where a one-dimensional color flux tube structure was assumed. Only qualitative considerations should be made while using the above potential at finite temperatures. The more accurate potential is necessary for quantitative comprehension and should be obtained directly from

QCD at finite temperature, much as the Cornell potential at zero temperature was obtained from pNRQCD using the zeroth-order matching coefficient.

In Ref. [134], Guo, Dong, Pan, and Moldes speculated that entropy could play a role in the interquark interaction. Their heuristic reasoning, which relies on associating thermodynamic quantities with the real part of the potential, led them to propose the in-medium string part as

$$V^{GDPM}(r,T) = \frac{2\sigma}{m_D}(1 - e^{-m_D r}) - \sigma r e^{-m_D r}. \tag{2.4}$$

Recently, a rigorous derivation of the generalized Gauss law for in-medium quarkonium in a complex potential model integrating the nonperturbative aspects of the vacuum-bound state with a weak coupling description of the medium degrees of freedom was presented in Ref [135].

In this thesis, we follow the method developed by the authors in Ref. [132, 136]. The foundation of potential models is the idea that a potential can adequately describe the interaction between a heavy quark and its anti-quark. We begin with the previously addressed Cornell potential at $T = 0$. The Fourier transform of the heavy quark potential is where the medium modification enters as

$$\tilde{V}(p) = \frac{V(p)}{\epsilon(p)}, \tag{2.5}$$

where $V(p)$ is the Fourier transform of the Cornell potential, which has to be regularized. We regulate both terms in the Cornell potential by multiplying with an exponential damping factor, and it is switched off after the Fourier transform is evaluated. Therefore, the Fourier transform is

$$V(p) = -\sqrt{2/\pi}\frac{\alpha}{p^2} - \frac{4\sigma}{\sqrt{2\pi}p^4}. \tag{2.6}$$

The inverse of dielectric permittivity $\epsilon^{-1}(p)$ is pertained to the temporal part of the effective gluon propagator $D^{\mu\nu}$ by definition given in Ref. [186]

$$\epsilon^{-1}(\boldsymbol{p}) = -\lim_{\omega \to 0} p^2 D^{00}(\omega, \boldsymbol{p}), \tag{2.7}$$

where $p = |\boldsymbol{p}|$. The propagator in the presence of a thermal medium can be expressed as

$$D_{\mu\nu}^{-1} = (D_{\mu\nu}^0)^{-1} - \Pi_{\mu\nu}, \tag{2.8}$$

where the $\Pi_{\mu\nu}$ is the gluon self-energy and the $D_{\mu\nu}^0$ is the bare gluon propagator. The gluon self-energy tensor can be decomposed in terms of two scalar functions, the longitudinal (Π^L) and transverse (Π^T) self-energies,

$$\Pi_{\mu\nu}(P) = -\Pi^T(P)T_{\mu\nu} + \frac{P^2}{p^2}\Pi^L(P)L_{\mu\nu}, \tag{2.9}$$

where $P = (\omega, \boldsymbol{p})$ and the tensors $T_{\mu\nu}$ and $L_{\mu\nu}$ are

$$T_{\mu\nu} = g_{\mu\nu} - \frac{P_\mu P_\nu}{P^2} - \frac{n_\mu n_\nu}{n^2} \quad \text{and} \quad L_{\mu\nu} = \frac{n_\mu n_\nu}{n^2}. \tag{2.10}$$

The four-vector n_μ is

$$n_\mu = n_\mu - \frac{n \cdot P}{P^2}P_\mu. \tag{2.11}$$

and satisfies $P.n = 0$ and $n^2 = 1 - (n.P)^2/P^2$. In three dimensions, the static limit pertains to the screening of fields, and the transverse component in the static limit $\Pi^T(0, p \to 0, T)$ vanishes; therefore, the gluon and ghost contribution to the longitudinal component of the self-energies is reduced to

$$\Pi_g^L(\omega, \boldsymbol{p}) = m_{Dg}^2 \left[1 - \frac{\omega}{2p} \ln\left(\frac{\omega + p}{\omega - p}\right) + i\pi \frac{\omega}{2p}\Theta(p^2 - \omega^2) \right]. \tag{2.12}$$

The above Eq. 2.12 can be rewritten in terms of real and imaginary parts as

$$\begin{aligned}
\Re\Pi_g^L(\omega, \boldsymbol{p}) &= m_{Dg}^2\left[1 - \frac{\omega}{2p}\ln\left(\frac{\omega+p}{\omega-p}\right)\right], \\
\Im\Pi_g^L(\omega, \boldsymbol{p}) &= m_{Dg}^2\frac{\pi\omega}{2p}\Theta(p^2 - \omega^2).
\end{aligned} \tag{2.13}$$

The total longitudinal component of gluon self-energy is the sum of the gluon and quark contribution

$$\Pi^L(\omega_n, \boldsymbol{p}) = \Pi_g^L(\omega_n, \boldsymbol{p}) + \Pi_q^L(\omega_n, \boldsymbol{p}), \tag{2.14}$$

36

which can be written in terms of real and imaginary parts. We compute the gluon self-energy's real and imaginary parts in the static limit ($\omega \to 0$). The real part of self-energy reads

$$\Re\Pi^L(\omega, \boldsymbol{p}) = \Re\Pi_g^L(\omega, \boldsymbol{p}) + \Re\Pi_q^L(\omega, \boldsymbol{p}), \tag{2.15}$$

and the imaginary part of the self-energy $\Im\Pi^L$ reads

$$\Im\Pi^L(\omega, \boldsymbol{p}) = \Im\Pi_g^L(\omega, \boldsymbol{p}) + \Im\Pi_q^L(\omega, \boldsymbol{p}). \tag{2.16}$$

The imaginary contribution from the quark loop can be obtained by using the identity

$$\Im\Pi_{n,q}^L(\omega_n, \boldsymbol{p}) = \frac{1}{2i} \lim_{\varepsilon \to 0} \left[\Pi_q^L(\omega_n + i\varepsilon, \boldsymbol{p}) - \Pi_q^L(\omega_n - i\varepsilon, \boldsymbol{p}) \right]. \tag{2.17}$$

Further, we compute both the real and imaginary part of the longitudinal component of the gluon propagator using the gluon self-energy. The spectral function approach, as defined in Ref. [139], is used to obtain the imaginary part of the gluon propagator as

$$\Im D^L(\omega, \boldsymbol{p}) = -\pi(1 + e^{-\beta\omega})\mathrm{A}^{\mathrm{L}}, \tag{2.18}$$

where A^{L} is defined as

$$\mathrm{A}^{\mathrm{L}}(\omega, \boldsymbol{p}) = \frac{1}{\pi} \frac{e^{\beta\omega}}{e^{\beta\omega} - 1} \rho^{\mathrm{L}}(\omega, \boldsymbol{p}). \tag{2.19}$$

The spectral function ρ^L can be expressed in the Breit-Wigner form as

$$\rho^L(\omega_n, \boldsymbol{p}) = \frac{\Im\Pi^L(\omega_n, \boldsymbol{p})}{(p^2 - \Re\Pi^L(\omega_n, \boldsymbol{p}))^2 + \Im\Pi^L(\omega_n, \boldsymbol{p})^2}. \tag{2.20}$$

After substituting Eq. (2.20) in Eq. (2.18), we obtain the longitudinal component of the gluon propagator, D^L in terms of real and imaginary parts. In the static ($\omega \to 0$) and massless light quark limit, we obtain

$$D^L(\boldsymbol{p}) = \frac{-1}{p^2 + \Pi^L(\boldsymbol{p})} + \frac{i\pi T \, \Pi^L(\boldsymbol{p})}{p(p^2 + \Pi^L(\boldsymbol{p}))^2}. \tag{2.21}$$

Using the gluon propagator, we obtain the dielectric permittivity as [136, 141, 186]

$$\epsilon^{-1}(\boldsymbol{p}) = \frac{p^2}{p^2 + \Pi^L} - i\pi T \frac{p\,\Pi^L}{(p^2 + \Pi^L)^2}, \tag{2.22}$$

where $\Pi^L \equiv \Pi^L(\boldsymbol{p})$ and

$$\lim_{p \to 0} \Pi = g^2 T^2 \left(\frac{N_c}{3} + \frac{N_f}{6} \right) \equiv m_D^2. \tag{2.23}$$

We use the dielectric permittivity expression Eq. (2.22) to compute the in-medium heavy quarkonium complex potential in an arbitrary magnetic field. Given that the static limit of the self-energy is momentum-independent, the pole of the inverse dielectric permittivity corresponds to the gauge-invariant Debye mass. This leads to an exponential damping of the potential. When non-perturbative phenomena like string tension are present, which persists even above the deconfinement point, the dependence of Debye mass on dielectric function may change. But for the Debye screened Coulomb and string part of the potential, we take the same screening mass scale m_D.

2.2.2 Real Part of the Potential

By correcting its short- and long-distance parts using a dielectric function $\epsilon(p)$ that accounts for the effects of deconfinement, one can deduce the modifications to the vacuum potential in the medium [141] as follows:

$$V(\boldsymbol{r}, T) = \int \frac{d^3\boldsymbol{p}}{(2\pi)^{3/2}} \left(e^{i\boldsymbol{p}.\boldsymbol{r}} - 1 \right) \frac{V(\boldsymbol{p})}{\epsilon(p)}, \tag{2.24}$$

where the heavy quark free energy has been renormalized by subtracting r-independent terms, which is the perturbative free energy of quarkonia at infinite separation. The real part of the potential can be derived from Eq. (2.24) by substituting the dielectric permittivity $\epsilon(p)$.

It's important to note that this one-loop result in linear response theory is perturbative, and the linear approximation in QCD is valid as long as the mean-field four-potential $\left(A_\mu^a \right)$

is significantly smaller than the temperature. Substituting the real part of permittivity, we obtain the medium-modified potential as,

$$
\begin{aligned}
\Re V(r,T) &= \int \frac{d^3\boldsymbol{p}}{(2\pi)^{3/2}} \left(e^{i\boldsymbol{p}.\boldsymbol{r}} - 1\right) \left(-\sqrt{(2/\pi)}\frac{\alpha}{p^2} - \frac{4\sigma}{\sqrt{2\pi}p^4}\right) \left(\frac{p^2}{(p^2 + m_D^2)}\right) \\
&\equiv \Re V_\alpha(r,T) + \Re V_\sigma(r,T),
\end{aligned}
\tag{2.25}
$$

Here, $\Re V_\alpha(r,T)$ and $\Re V_\sigma(r,T)$ represent the medium modifications of the Coulomb and string terms, respectively. Upon performing the momentum integration, the Coulomb term transforms into

$$
\Re V_\alpha(r,T) = -\alpha m_D \left(\frac{e^{-\hat{r}}}{\hat{r}} + 1\right).
\tag{2.26}
$$

The string term is simplified into

$$
\Re V_\sigma(r,T) = \frac{2\sigma}{m_D} \left(\frac{(e^{-r} - 1)}{\hat{r}} + 1\right).
\tag{2.27}
$$

The real part of the potential then becomes (with $\hat{r} = rm_D$)

$$
\Re V(\hat{r},T) = \left(\frac{2\sigma}{m_D} - \alpha m_D\right)\frac{e^{-\hat{r}}}{\hat{r}} - \frac{2\sigma}{m_D\hat{r}} + \frac{2\sigma}{m_D} - \alpha m_D.
\tag{2.28}
$$

This potential is found to include an additional long-range Coulomb term, supplementing the conventional Yukawa term. In the short-distance limit ($\hat{r} \ll 1$), the above potential approaches the Cornell potential, meaning the $Q\bar{Q}$-pair does not perceive the medium. However, at large distances ($\hat{r} \gg 1$), the potential simplifies, especially under the high-temperature approximation (i.e., where $\sigma/m_D(T)$ can be neglected):

$$
\Re V(r,T) \approx -\frac{2\sigma}{m_D^2 r} - \alpha m_D.
\tag{2.29}
$$

Aside from a constant term, this expression resembles a Coulomb-like potential, with the identification of $2\sigma/m_D^2$ as the square of the strong coupling (g^2).

2.2.3 Imaginary part of the potential

Lattice QCD suggests that at finite temperature, as one transitions into the deconfined phase, the real part not only gradually weakens but also reveals the existence of a finite imaginary part beyond the pseudocritical temperature [137, 138]. The bound state peak can be made weaker or reduced to a threshold enhancement by altering the imaginary part of the potential. This leads to a finite thermal width (Γ) for the resonance peak in the spectral function, determining the dissociation temperature. Dissociation is expected to occur when the binding energy decreases with temperature and becomes equal to Γ. The imaginary part of the dielectric function in the medium from Eq. 2.22 is

$$\Im\epsilon^{-1}(p) = -\pi T m_D^2 \frac{p^2}{p\left(p^2 + m_D^2\right)^2}. \tag{2.30}$$

Similarly, the imaginary part of the potential can be determined using the definition of the potential given in Eq. (2.24). The medium modification to the short-distance and long-distance terms are

$$\Im V_\alpha(r, T) = -\frac{\alpha}{2\pi^2} \int d^3 \boldsymbol{p} \left(e^{i\boldsymbol{p}\cdot\boldsymbol{r}} - 1\right) \left[\frac{\pi T m_D^2}{p\left(p^2 + m_D^2\right)^2}\right],$$

$$\Im V_\sigma(r, T) = -\frac{4\sigma}{(2\pi)^2} \int \frac{d^3 \boldsymbol{p}}{(2\pi)^{3/2}} \left(e^{i\boldsymbol{p}\cdot\boldsymbol{r}} - 1\right) \frac{1}{p^2} \left[\frac{\pi T m_b^2}{p\left(p^2 + m_D^2\right)^2}\right]. \tag{2.31}$$

Following the integration, the contribution from the Coulomb term to the imaginary part is given by (with $z = p/m_D$)

$$\Im V_\alpha(r, T) = -2\alpha T \int_0^\infty \frac{dz}{(z^2 + 1)^2} \left(1 - \frac{\sin z\hat{r}}{z\hat{r}}\right)$$

$$\equiv -\alpha T \phi_0(\hat{r}), \tag{2.32}$$

and the contribution due to the string term becomes

$$\Im V_\sigma(r, T) = \frac{4\sigma T}{m_D^2} \int_0^\infty \frac{dz}{z\left(z^2 + 1\right)^2} \left(1 - \frac{\sin z\hat{r}}{z\hat{r}}\right)$$

$$\equiv \frac{2\sigma T}{m_D^2} \psi_0(\hat{r}), \tag{2.33}$$

40

where the functions, $\phi_0(\hat{r})$ and $\psi_0(\hat{r})$ at leading-order in $\hat{r}$ are

$$\phi_0(\hat{r}) = -\frac{\hat{r}^2}{9}\left(-4 + 3\gamma_E + 3\log\hat{r}\right)$$
$$\psi_0(\hat{r}) = \frac{\hat{r}^2}{6} + \left(\frac{-107 + 60\gamma_E + 60\log(\hat{r})}{3600}\right)\hat{r}^4 + O\left(\hat{r}^5\right). \tag{2.34}$$

In the limit of short distances ($\hat{r} \ll 1$), both contributions, at the leading logarithmic order, reduce to

$$\Im V_\alpha(r, T) = -\alpha T\frac{\hat{r}^2}{3}\log\left(\frac{1}{\hat{r}}\right),$$
$$\Im V_\sigma(r, T) = -\frac{2\sigma T}{m_D^2}\frac{\hat{r}^4}{60}\log\left(\frac{1}{\hat{r}}\right). \tag{2.35}$$

Therefore, the sum of the Coulomb and string terms provides the imaginary part of the potential in the medium:

$$\Im V(r, T) = -T\left(\frac{\alpha\hat{r}^2}{3} + \frac{\sigma\hat{r}^4}{30m_D^2}\right)\log\left(\frac{1}{\hat{r}}\right). \tag{2.36}$$

It is immediately evident that for short distances, the imaginary part vanishes. Furthermore, its magnitude is greater than when only the Coulombic term is considered, thereby amplifying the thermal width of the resonances in the thermal medium.

Chapter 3

Liénard–Wiechert potential of quarkonia in QGP

Drawing upon the research conducted by Jobin Sebastian, Mohammad Yousuf Jamal, and Najmul Haque, as presented in *Phys.Rev.D* **107** (2023) 5, 054040.

This chapter delves into the characteristics of the complex retarded potential of a heavy quarkonium traversing a hot and dense, stationary QGP medium. Drawing inspiration from the well-established notion of the retarded potential in electrodynamics, we extend this notion to heavy quarkonium, changing the static vacuum Cornell potential through Lorentz transformation to the static frame of the QGP. The consequent potential in the vacuum is further refined to account for the screening effect introduced by the thermal medium. To achieve this, the dielectric function of the static QGP medium modifies the retarded Cornell potential. We present the analytical formulation of the potential, approximated under a small velocity limit, and provide numerical results for the real and imaginary components of the potential. Considering the relative motion of a heavy quarkonium with respect to the static QGP medium, we move beyond the spherical symmetry assumption for the potential. We examine the angular dependence of the real and imaginary parts of the potential at various velocities. Our observations reveal that the potential is more responsive to temperature when the velocity is low, while it becomes highly sensitive to velocity in the relativistic regime. Additionally, we note that the string term weakens the screening of the potential compared to the Coulombic part alone, both in real and imaginary cases. Finally, we explore the thermal width of quarkonia in the QGP medium, calculated using the imaginary

part of the potential, and investigate its dependence on velocity and temperature.

3.1   Context and Objectives

In the preceding chapter, we explored the temperature dependence of the quarkonium potential. This chapter focuses on the velocity dependence of the potential for heavy quarkonia moving in a QGP medium. Our objective is to investigate the potential in a scenario where the QGP medium is static and uniform while the heavy quarkonia are in motion relative to the rest frame of the medium. This scenario mirrors the situation of the retarded potential of a moving charged particle in electromagnetic plasma or the general Liénard-Wiechert potential in the context of QCD. The outcomes derived in this static and uniform medium context do not necessarily directly translate to a clean suppression signal in a rapidly expanding QGP. However, it serves the purpose of capturing the relative motion between heavy quarkonia and the QGP medium, introducing a departure from the spherical symmetry of the potential. This analysis aids in understanding the modification of the binding of quark and antiquark pairs, subsequently influencing the survival probabilities of quarkonia states observed in an asymmetric emission pattern in anisotropic flow.

The motivation behind this study is to explore the interplay of temperature, screening, and velocity on the retarded potential of moving quarkonia in a static QGP medium, examining its angular dependence during motion. In this work, we establish a framework for studying the Liénard–Wiechert/retarded potential of a heavy quark, leading to the potential for quarkonium-bound states inside the QGP. To achieve this, we express the Cornell potential in a covariant form and subsequently perform a Lorentz transformation to transition to the static QGP frame where the heavy quark is in motion. This potential is then modified using the dielectric permittivity of the QGP medium, revealing both the real and imaginary parts of the retarded potential. It's important to note that this chapter primarily

focuses on studying chromoelectric interactions, excluding considerations of color magnetic field effects. Within this framework, we investigate the complete angular dependence of the retarded potential, presenting corresponding plots in the results section. Alongside the derivation of the analytical expression within the small velocity limit, we provide full numerical results to assess the validity of the assumption. Furthermore, we leverage the imaginary part of the potential to calculate the thermal width of quarkonia and explore its dependence on velocity and temperature.

3.2   Retarded Cornell potential

Establishing a correspondence with QED aids in maintaining theoretical consistency, enhancing our understanding of the hot QCD medium. Particularly, the QED plasma bears resemblance to the QCD plasma in specific cases, such as at the soft scale where the field fluctuation is on the order of $\sqrt{g}$ and characterized by a small coupling [140]. In this context, we draw upon the analogy of the Liénard–Wiechert potential from electrodynamics, extending it to derive the retarded potential for heavy quarkonium within the QGP medium. We commence by considering the (static) Cornell potential that governs the binding of the quark-antiquark pair in a vacuum, expressing it in a covariant form. Subsequently, we apply Lorentz transformations to observe how the four-potential in a particular frame transforms into any other frame, enriching our insight into the dynamics of heavy quarkonium in the QGP medium. The four-potential corresponds to heavy quark-antiquark interaction in its rest frame with the Cornell potential as the scalar part is given by

$$A_0^\mu = \left(-\frac{\alpha}{r} + \sigma r, \mathbf{0} \right), \tag{3.1}$$

where $r = |\boldsymbol{r}|$ is the distance from heavy quark to the field point; $\alpha = C_F \alpha_s$ with $C_F = \left(N_c^2 - 1 \right) / 2 N_c$ and α_s is the strong coupling constant, σ is the string tension, and N_c is the number of color degrees of freedom. The four-potential A_0^μ in Eq. (3.1) can be written in the

44

covariant form by introducing the four-velocity $u_0^\mu \equiv (1, \mathbf{0})$ in the rest frame of the heavy quark. So, in the rest frame of the quarkonium, the four-potential is

$$A_0^\mu = \left(-\frac{\alpha}{r_\nu u_0^\nu} + \sigma \, (r_\nu u_0^\nu), \mathbf{0} \right), \tag{3.2}$$

Note that $r_\nu u_0^\nu = r$. Now, the Lorentz transformations of Eq. (3.2) to a frame where the heavy quarkonia is moving with a velocity, $\boldsymbol{v}$ is given as

$$A^\mu = \gamma \left(-\frac{\alpha}{r_\nu u^\nu} + \sigma \, r_\nu u^\nu, -\frac{\alpha \boldsymbol{v}}{r_\nu u^\nu} + \sigma \boldsymbol{v} \, r_\nu u^\nu \right), \tag{3.3}$$

where $\gamma = 1/\sqrt{1 - v^2}$ is the Lorentz factor. Rewriting Eq. (3.3) in a more compact form, one gets

$$A^\mu = \left(-\frac{\alpha}{(r_\nu u^\nu)} + \sigma \, (r_\nu u^\nu) \right) u^\mu. \tag{3.4}$$

Here, r_μ is the position four-vector from the heavy quark $(t_r, \boldsymbol{x'})$ at retarded time to some field point $(t, \boldsymbol{x})$, and $u^\mu = \gamma(1, \boldsymbol{v})$ with $v = |\boldsymbol{v}|$. It is crucial to emphasize that the two events defining r_μ are linked by a signal propagating at the velocity of light. Consequently, these events exhibit null separation, rendering r_μ a light-like vector. The modified form of the Cornell potential, as indicated in Eq. (3.4), shares similarities with the Liénard–Wiechert potential in electrodynamics, albeit lacking the string part in the latter. Now we have,

$$r_\nu u^\nu = \gamma r - \gamma \boldsymbol{r} \cdot \boldsymbol{v} = r\gamma \left(1 - \hat{\boldsymbol{r}} \cdot \boldsymbol{v} \right), \tag{3.5}$$

where $\hat{\boldsymbol{r}}$ is the unit vector in the direction of $\boldsymbol{r}$. Then the scalar potential, *i.e.,* the zeroth component of the four-potential, can be written as

$$V_{\text{vac}}(\boldsymbol{r}, \boldsymbol{v}) = -\frac{\alpha}{r \left(1 - \hat{\boldsymbol{r}} \cdot \boldsymbol{v} \right)} + \gamma^2 \sigma \, r \left(1 - \hat{\boldsymbol{r}} \cdot \boldsymbol{v} \right). \tag{3.6}$$

This formalism remains valid even when the heavy quark velocity is nonuniform. The calculations in this section utilize a sequence of independent Lorentz transformations, each

executed at a different point along the trajectory of the particle. To address the scenario of a quarkonia traversing a QGP medium, we can assume the velocity to be constant. Furthermore, if we align our z-axis along the direction of velocity, then at $t = 0$,

$$r\left(1 - \hat{\boldsymbol{r}} \cdot \boldsymbol{v}\right) = \sqrt{z^2 + (1 - v^2)(x^2 + y^2)}. \tag{3.7}$$

Here, for convenience, the heavy quark is set to pass through the origin at $t = 0$ and uses the fact that r^μ is a light-like vector. Now using Eq. (3.7) in Eq. (3.6) the retarded potential in Cartesian coordinates becomes,

$$V_{\text{vac}}(x, y, z, v) = -\frac{\alpha}{\sqrt{z^2 + (1 - v^2)(x^2 + y^2)}} + \gamma^2 \sigma \sqrt{z^2 + (1 - v^2)(x^2 + y^2)}. \tag{3.8}$$

The modified retarded potential in the medium can be accomplished in Fourier space by dividing the potential by the dielectric permittivity. Consequently, the vacuum potential in Fourier space is written as

$$V_p(p_x, p_y, p_z, v) = -\sqrt{\frac{2}{\pi}} \left(\frac{\alpha}{p_x^2 + p_y^2 + (1 - v^2)\, p_z^2} - \frac{2\sigma}{\left[p_x^2 + p_y^2 + (1 - v^2)\, p_z^2\right]^2} \right). \tag{3.9}$$

In spherical polar coordinates, the above equation becomes

$$V_p(\boldsymbol{p}, v) = -\sqrt{\frac{2}{\pi}} \left(\frac{\alpha}{p^2 \left(1 - v^2 \cos^2 \theta\right)} - \frac{2\sigma}{p^4 \left(1 - v^2 \cos^2 \theta\right)^2} \right). \tag{3.10}$$

Here, θ represents the polar angle in momentum space, i.e., the angle between p_z and $\boldsymbol{p}$. This expression provides the retarded scalar potential of a moving quarkonium in the vacuum. As pointed out before, when the charged particle traverses a thermal medium, its properties are influenced by the response of that medium. Therefore, when a heavy quarkonium moves through the QGP medium (which is at rest in this scenario), the associated retarded potential will be influenced by the response of the QGP medium. Consequently, we will proceed to discuss the modification of the heavy quark potential given in Eq. (3.10) through the dielectric permittivity of the QGP medium in Fourier space.

3.3 Dielectric permittivity and the in-medium potential

The medium-modified potential in coordinate space $V(\boldsymbol{r}, v)$ is obtained [132, 136] by correcting the vacuum potential with the dielectric permittivity that encodes the medium screening property in Fourier space, followed by inverse Fourier transformation, *i.e.,*

$$V(\boldsymbol{r}, v) = \frac{1}{(2\pi)^{3/2}} \int d^3 \boldsymbol{p} \, (e^{i\boldsymbol{p}\cdot r} - 1) \, \frac{V_p(\boldsymbol{p}, v)}{\epsilon(p)}, \tag{3.11}$$

where $V_p(\mathbf{p}, v)$ is the Fourier transform of the potential in coordinate space and $\epsilon(p)$ is the dielectric permittivity of the medium. Here, we subtract the $\boldsymbol{r}-$independent terms in order to renormalize the heavy quark free energy [142]. The inverse of the dielectric permittivity of the static QGP medium is given as [124],

$$\epsilon^{-1}(p) = \frac{p^2}{p^2 + m_D^2} - i\pi T \frac{m_D^2 p}{(p^2 + m_D^2)^2}, \tag{3.12}$$

where $p = |\boldsymbol{p}|$ and m_D is the Debye mass of QGP medium obtained from the static limit of longitudinal polarisation tensor in the high-temperature limit [143],

$$m_D = T\sqrt{4\pi\alpha_s \left(\frac{N_f}{6} + \frac{N_c}{3}\right)}, \tag{3.13}$$

where N_f is the number of flavor degrees of freedom, and T is the temperature of the medium. Since the medium is assumed to be static, the Debye screening mass is only a function of temperature, and no modification of the screening of gluonic modes is required. We use one-loop strong coupling α_s as [144, 145],

$$\alpha_s = \frac{12\pi}{11N_c - 2N_f} \frac{1}{\ln(\Lambda/\Lambda_{\overline{MS}})^2}, \tag{3.14}$$

where $\Lambda_{\overline{MS}} = 176\text{MeV}$ is the QCD scale fixing factor and $\Lambda = 2\pi T$.

To calculate the exact real part of the potential, we decompose the potential into the Coulombic part and the string part, followed by performing separate integrations,

$$\Re V(\boldsymbol{r}, v) = \Re V_\alpha(\boldsymbol{r}, v) + \Re V_\sigma(\boldsymbol{r}, v). \tag{3.15}$$

The Coulombic part is written as

$$\Re V_\alpha(\boldsymbol{r}, v) = -\sqrt{\frac{2}{\pi}} \int \frac{d^3\boldsymbol{p}}{(2\pi)^{3/2}} \left(\frac{e^{i\boldsymbol{p}\cdot\boldsymbol{r}}}{p^2 + m_D^2} \frac{\alpha}{1 - v^2\cos^2\theta} - \frac{m_D^2}{p^2 + m_D^2} \frac{\alpha}{p^2(1 - v^2\cos^2\theta)} \right).$$
(3.16)

There are no diverging terms in the string part integration; therefore,

$$\Re V_\sigma(\boldsymbol{r}, v) = -\int \frac{d^3\boldsymbol{p}}{(2\pi)^3} (e^{i\boldsymbol{p}\cdot\boldsymbol{r}} - 1) \frac{1}{p^2 + m_D^2} \sqrt{\frac{2}{\pi}} \frac{2\sigma}{p^2(1 - v^2\cos^2\theta)^2}.$$
(3.17)

In spherical polar coordinates,

$$\boldsymbol{p} \cdot \boldsymbol{r} = rp \big[\sin\Theta \sin\theta \cos(\Phi - \phi) + \cos\Theta \cos\theta \big].$$

Here, the angles θ and ϕ denote the polar and azimuthal angles in Fourier space (momentum space), respectively, while Θ and Φ represent the polar and azimuthal angles in coordinate space. Given that the velocity of the heavy quark is along the z-axis, Θ signifies the angle between the velocity $\boldsymbol{v}$ and the position of the field point $\boldsymbol{r}$. The integration over the azimuthal angle, ϕ, can be carried out analytically, yielding:

$$\Re V(\boldsymbol{r}, v) = -\frac{1}{\pi} \int \frac{\sin\theta \, d\theta \, dp}{p^2 + m_D^2} \left[\frac{\alpha \left(m_D^2 + p^2 e^{ipr\cos\theta\cos\Theta} J_0(pr\sin\theta\sin\Theta) \right)}{1 - v^2\cos^2\theta} \right.$$
$$\left. - \frac{2\sigma \left(1 - e^{ipr\cos\theta\cos\Theta} J_0(pr\sin\theta\sin\Theta) \right)}{(1 - v^2\cos^2\theta)^2} \right], \quad (3.18)$$

where J_0 represents the Bessel's function of the first kind. The integration over p and θ in Eq. (3.18) can be computed numerically, and the real part of the potential is plotted in the figure 3.1. Similarly, the exact imaginary part of the potential is calculated by substituting the imaginary part of the dielectric function in Eq. (3.11),

$$\Im V(\boldsymbol{r}, v) = \int \frac{d^3\boldsymbol{p}}{(2\pi)^{3/2}} (e^{i\boldsymbol{p}\cdot\boldsymbol{r}} - 1) \frac{\pi T m_D^2 p}{(p^2 + m_D^2)^2}$$
$$\times \sqrt{\frac{2}{\pi}} \left[\frac{\alpha}{p^2(1 - v^2\cos^2\theta)} + \frac{2\sigma}{p^4(1 - v^2\cos^2\theta)^2} \right]. \quad (3.19)$$
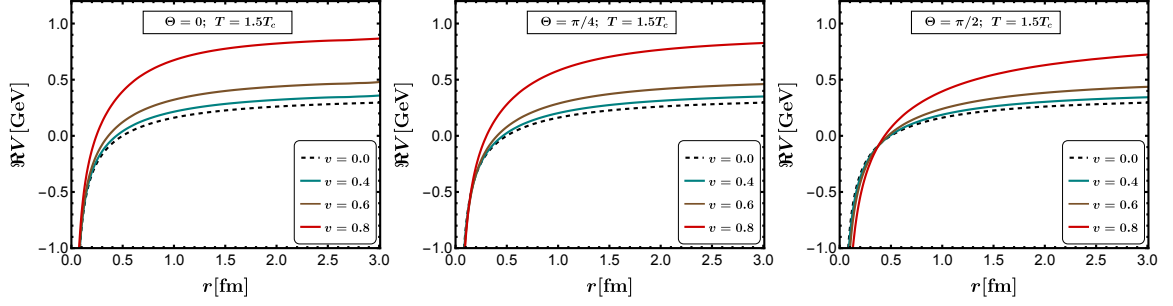
Figure 3.1: Numerical results obtained for the real part of the potential at various velocities and angles ($\Theta = 0$ (left), $\Theta = \pi/4$ (middle), $\Theta = \pi/2$ (right)).
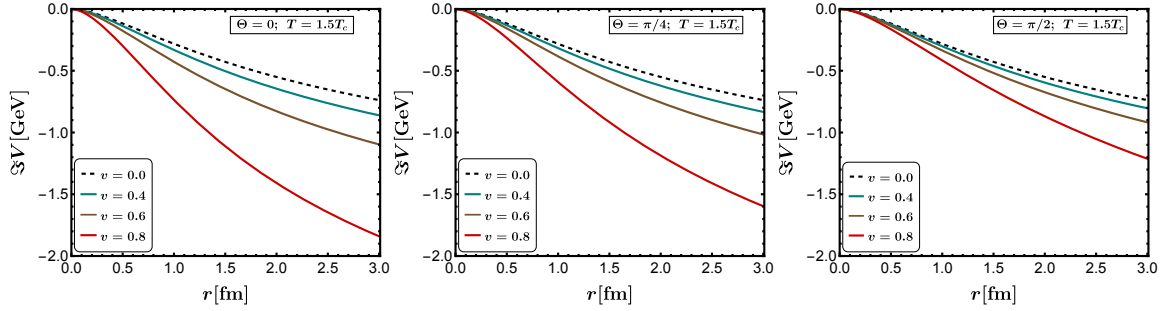
Figure 3.2: Numerical results obtained for the imaginary part of the potential at various velocities and angles ($\Theta = 0$ (left), $\Theta = \pi/4$ (middle), $\Theta = \pi/2$ (right)).

After integrating over ϕ we obtain,

$$\Im V(\boldsymbol{r}, v) = -m_D^2 T \int \frac{\sin\theta \, d\theta \, dp}{\left(p^2 + m_D^2\right)^2} \left[\frac{\alpha p}{1 - v^2\cos^2\theta} + \frac{2\sigma}{p\left(1 - v^2\cos^2\theta\right)^2} \right] \times \left\{ 1 - e^{ipr\cos\theta\cos\Theta} J_0(pr\sin\theta\sin\Theta) \right\}. \tag{3.20}$$

The potentials' real and imaginary parts are independent of Φ after ϕ integration, *i.e.,* potential has axial symmetry about the z-axis. The rest of the integration is done numerically, and the results are plotted as shown in the figure for both real (figure 3.1) and imaginary (figure 3.2) parts of the potential.
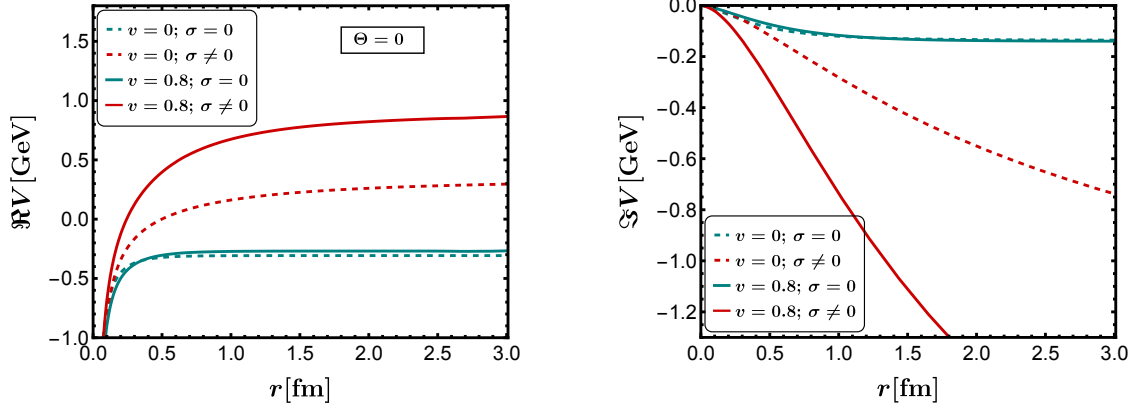
Figure 3.3: Numerical results obtained for real (left) and imaginary (right) parts of the potential, a comparison between Cornell and Coulomb potentials.
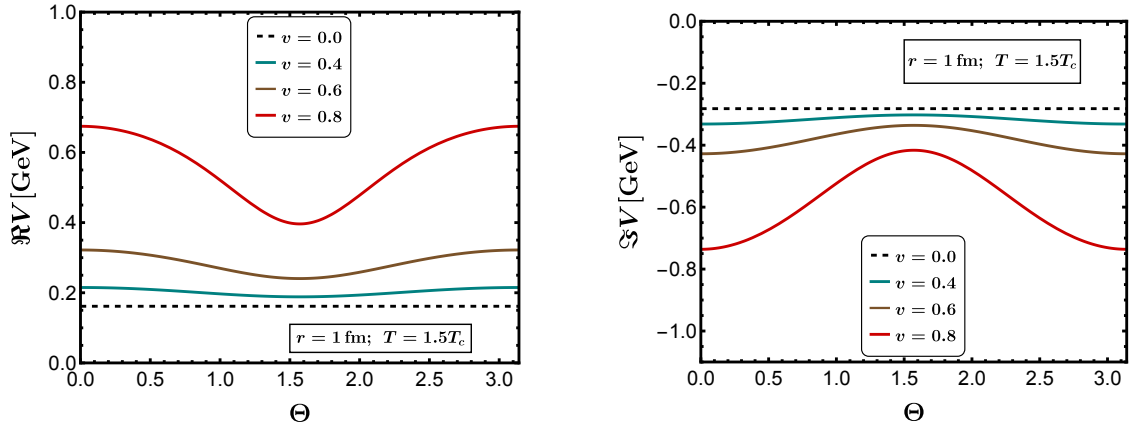
Figure 3.4: Numerical results obtained for the angular variation of real (left) and imaginary (right) parts of the potential at various velocities. Here, Θ is in units of radian

3.4 Potential at small velocities

The real and imaginary parts of the potential as obtained in Eqs. (3.18) and Eq. (3.20) can be simplified at small velocities. Considering small velocity, one can expand the $V_p(\boldsymbol{p}, v)$ in Eq. (3.10) and keep terms up to $O\left(v^2\right)$ as,

$$\frac{1}{1 - v^2 \cos^2 \theta} \approx 1 + v^2 \cos^2 \theta + O\left(v^4\right). \tag{3.21}$$
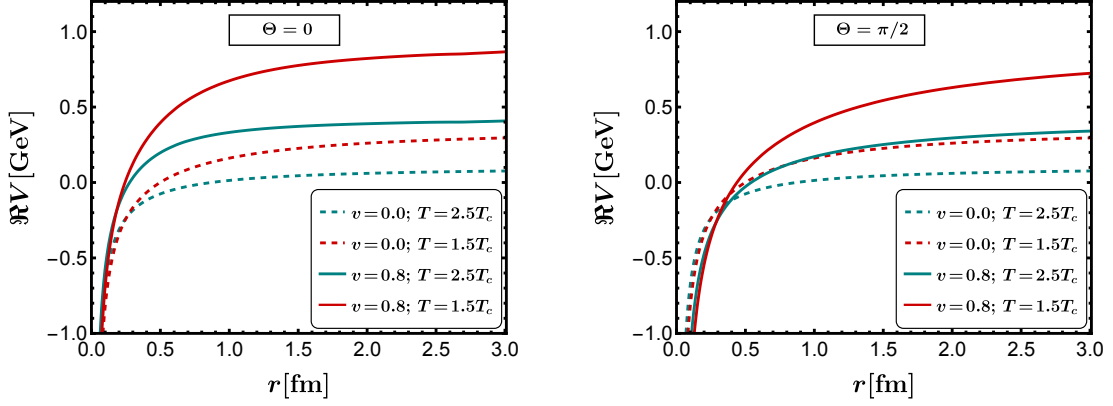
Figure 3.5: Numerical results obtained for the real part of the potential at various temperatures and velocities, a comparison.
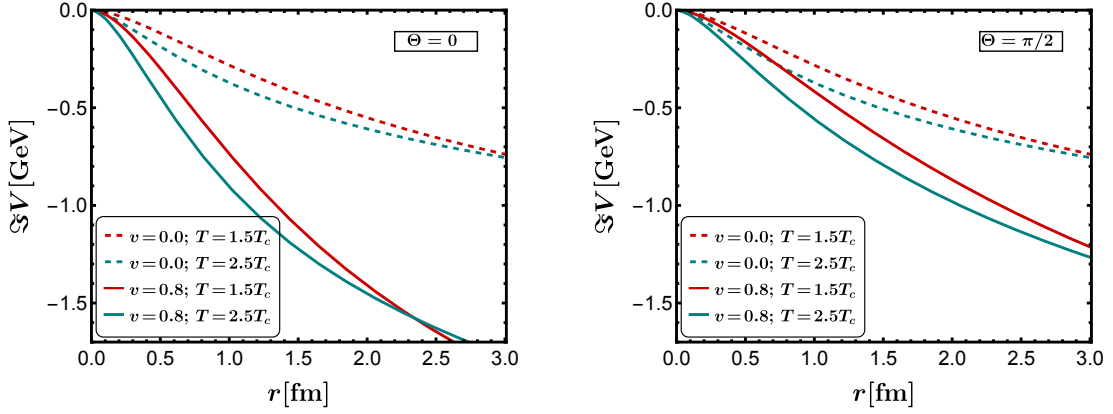
Figure 3.6: Numerical results obtained for the imaginary part of the potential at various temperatures and velocities, a comparison.

This approximation is valid for the case of a quarkonia moving in the QGP medium with a relatively small velocity. Next, we can analytically perform the integration in Eq. (3.11) using the approximation given in Eq. (3.21) to obtain the real part and imaginary part of the potential. The modified form of the potential in Eq. (3.10) in small velocity limit is

$$V_p(p, \theta, v) = -\sqrt{\frac{2}{\pi}} \frac{1}{p^2} \left(\alpha + \alpha v^2 \cos^2 \theta + \frac{2\sigma}{p^2} + \frac{4\sigma v^2 \cos^2 \theta}{p^2} \right). \tag{3.22}$$

Therefore, the real part of the potential at a small velocity is obtained as

$$\Re V(\boldsymbol{r}, v) = \int \frac{d^3 \boldsymbol{p}}{(2\pi)^{3/2}} \left(e^{i\boldsymbol{p} \cdot \boldsymbol{r}} - 1 \right) V_p(p, \theta, v) \mathrm{Re}[\epsilon^{-1}(\mathbf{p})]. \tag{3.23}$$

The integration in Eq. (3.23) is easy to calculate in spherical polar coordinates with $\cos\theta = p_z/p$. Doing so, the real part of the potential is computed as,

$$
\begin{aligned}
\Re V(\rho, \Theta, v) \approx &-\frac{\alpha m_D e^{-\rho}}{\rho} - \alpha m_D - \frac{2\sigma}{m_D\rho}\left(1 - e^{-\rho}\right) + \frac{2\sigma}{m_D} - \frac{\alpha v^2 m_D}{3} + \frac{4\sigma v^2}{3m_D} \\
&- \frac{\alpha m_D v^2}{\rho^3}\left(1 - 3\cos^2\Theta\right) + \frac{\alpha m_D v^2 e^{-\rho}}{\rho}\left\{\frac{1}{\rho} + \frac{1}{\rho^2} - \left(1 + \frac{3}{\rho} + \frac{3}{\rho^2}\right)\cos^2\Theta\right\} \\
&- \frac{2\sigma v^2}{m_D\rho}\left(1 - \cos^2\Theta\right) + \frac{4\sigma v^2}{m_D\rho^3}\left(1 - 3\cos^2\Theta\right) \\
&+ \frac{4\sigma v^2 e^{-\rho}}{m_D\rho}\left(\cos^2\Theta - \frac{1 - 3\cos^2\Theta}{\rho} - \frac{1 - 3\cos^2\Theta}{\rho^2}\right),
\end{aligned}
\tag{3.24}
$$

where $\rho = m_D r$. At $v = 0$, the approximate real part of the potential in Eq. (3.24) becomes the more familiar screened Cornell potential where the angular dependence has also disappeared,

$$
\Re V(r)|_{v=0} = -\frac{\alpha e^{-m_D r}}{r} - \alpha m_D - \frac{2\sigma}{m_D^2 r}\left(1 - e^{-m_D r}\right) + \frac{2\sigma}{m_D}.
\tag{3.25}
$$

The screened Cornell potential at $v = 0$ further converges to the vacuum Cornell potential as $m_D \to 0$ with $T \to 0$, we have

$$
\Re V(r)|_{v=0; T=0} = -\frac{\alpha}{r} + \sigma r.
\tag{3.26}
$$

Similarly, the imaginary part of the retarded potential in the small velocity approximation can be obtained as,

$$
\Im V(\boldsymbol{r}, v) = \int \frac{d^3\boldsymbol{p}}{(2\pi)^{3/2}}\left(e^{i\boldsymbol{p}\cdot\boldsymbol{r}} - 1\right)V_p(p, \theta, v)\text{Im}[\epsilon^{-1}(\mathrm{p})].
\tag{3.27}
$$

After performing the ϕ and the θ integration, we obtain the following results for the imaginary part of the potential. For the static case, the potential is isotropic, and it is obtained as

$$
\begin{aligned}
\Im V_{\text{iso}} = &-2\alpha T \int\limits_0^\infty \frac{z}{(z^2 + 1)^2}\left[1 - \frac{\sin(m_D r z)}{m_D r z}\right] dz \\
&- \frac{4\sigma T}{m_D^2} \int_0^\infty \frac{dz}{z\,(z^2 + 1)^2}\left[1 - \frac{\sin(m_D r z)}{m_D r z}\right],
\end{aligned}
\tag{3.28}
$$

where $z = p/m_D$. In the small velocity limit, the imaginary part of the potential can be expressed as [136, 146]

$$\Im V = \mathcal{A}(r, T, v) + \mathcal{B}(r, T, v) \cos(2\Theta). \tag{3.29}$$

In general, one can proceed with any angle Θ and evaluate the integration over p numerically. Here we are showing the results for $\Theta = 0$ (parallel case) and $\Theta = \pi/2$ (perpendicular case) in a small velocity limits as

$$\Im V^{\parallel}(v, r) = \Im V_{\text{iso}} + \frac{2}{3} v^2 T \left(\frac{\alpha}{3} \int_0^\infty \frac{z \, dz}{(z^2 + 1)^2} + \frac{4\sigma}{m_D^2} \int_0^\infty \frac{dz}{z (z^2 + 1)^2} \right)$$
$$\times \left[1 - \frac{3\sin(\rho z)}{\rho z} - \frac{6\cos(\rho z)}{\rho^2 z^2} + \frac{6\sin(\rho z)}{\rho^3 z^3} \right], \tag{3.30}$$

and

$$\Im V^{\perp}(v, r) = \Im V_{\text{iso}} + \frac{2}{3} v^2 T \left(\frac{\alpha}{3} \int_0^\infty \frac{z \, dz}{(z^2 + 1)^2} + \frac{4\sigma}{m_D^2} \int_0^\infty \frac{dz}{z (z^2 + 1)^2} \right)$$
$$\times \left[1 + \frac{3\cos(\rho z)}{\rho^2 z^2} - \frac{3\sin(\rho z)}{\rho^3 z^3} \right]. \tag{3.31}$$

Therefore, we can write

$$\mathcal{A}(r, T, v) = \left[\Im V^{\parallel}(v, r) + \Im V^{\perp}(v, r) \right] / 2 \tag{3.32}$$

and

$$\mathcal{B}(r, T, v) = \left[\Im V^{\parallel}(v, r) - \Im V^{\perp}(v, r) \right] / 2. \tag{3.33}$$

It is evident from Eq. (3.30) and Eq. (3.31) that at $v = 0$, the approximate imaginary part of the potential will contain only the isotropic part given in Eq. (3.28), which also vanishes in the vacuum as $T \to 0$. That means only the Cornell potential given in Eq. (3.1) remains after taking the limit $v \to 0$ and $T \to 0$, the original potential we started with.

3.5 Thermal Width

The thermal width of the quarkonium resonant state can be investigated using the imaginary part of the potential. Assuming the imaginary part of the potential as the perturbation to the vacuum potential, we calculate the thermal width in the first order of perturbation, as outlined in previous studies [133, 147, 148]

$$\Gamma_{Q\bar{Q}}(v) = -\langle \Psi | \Im V(v, r, \Theta) | \Psi \rangle, \tag{3.34}$$

where $\Psi(r)$ represents the wave function of the quarkonium bound states. Considering that the dominant contribution to the potential for deeply bound quarkonium states in QGP is Coulombic, the hydrogen atom wave function serves as a suitable approximation for calculating the thermal width of quarkonium-bound states. Consequently, the quarkonium wave function in the QGP frame is given by ground state hydrogen atom wavefunction [141] as

$$\Psi(r) = \frac{1}{\sqrt{\pi a_0^3}} e^{-q/a_0}, \tag{3.35}$$

where $q = r\sqrt{1 + \frac{v^2 \cos^2 \Theta}{1 - v^2}}$ is due to the Lorentz transformation of the wave function, $a_0 = 2/(C_F m_Q \alpha_s)$ is the Bohr radius corresponds to the quarkonia and m_Q is the quark mass. Note that one can get the exact wave function solving the Schrödinger equation with the real part of the potential (3.18), and we intend to do that in the near future. Substituting Eq. (3.35) in Eq. (3.34) gives

$$\Gamma_{Q\bar{Q}}(v) = -\frac{1}{\pi a_0^3} \int d^3 r \, e^{-2q/a_0} \Im V(r, v, \Theta). \tag{3.36}$$

Here, we obtain the exact results using full imaginary potential given in Eq. (3.20) as

$$\Gamma_{Q\bar{Q}}(v) = \frac{2m_D^2 T}{a_0^3} \int dr \, d\Theta \, r^2 \sin \Theta \, e^{-2q/a_0} \int \frac{\sin \theta \, d\theta \, dp}{(p^2 + m_D^2)^2}$$
$$\times \left[\frac{\alpha p}{1 - v^2 \cos^2 \theta} + \frac{2\sigma}{p(1 - v^2 \cos^2 \theta)^2} \right]. \tag{3.37}$$
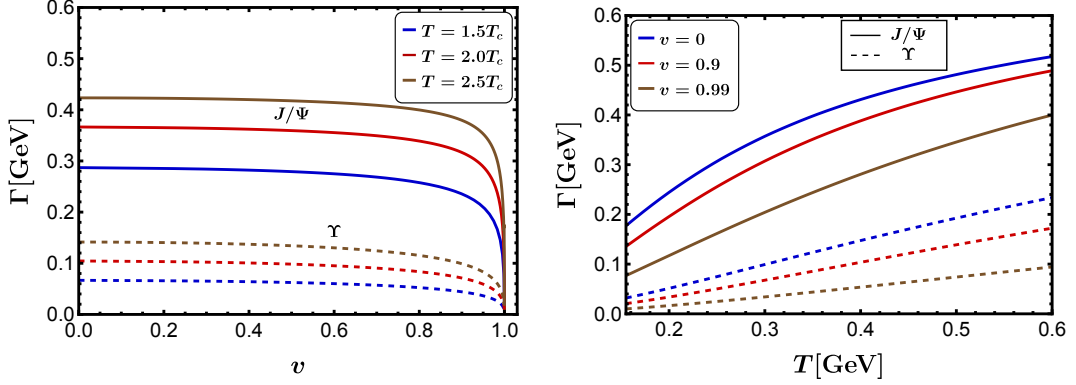
Figure 3.7: Decay width of the $J/\psi(1s)$ and $\Upsilon(1s)$ with velocity (left) and temperature (right).

Graphs depicting the thermal width of charmonium and bottomonium ground states are presented, showcasing their dependence on temperature and velocity. The derived expression serves as the basis for these plots, and a detailed discussion follows in the subsequent results sections.

3.6   Results and discussions

The heavy-quarkonium potential in the QGP medium is studied analytically and numerically with respect to various parameters, primarily the quarkonia velocity and angular dependence. The thermal width of the quarkonium ground state is obtained, and its dependence on velocity and temperature is studied. The illustration of results in various plots used different temperature $T = 1.5\,T_c$, $2\,T_c$, and $2.5\,T_c$ where the crossover temperature, $T_c = 0.155$ GeV. The number of quark flavors $N_f = 3$ and $\sigma = 0.18$ GeV^2. The temperature dependence in the potential arises through the strong coupling (α_s), the dielectric function $\epsilon(p)$, and Debye mass (m_D).

Figure 3.1 shows the variation of the real part of the potential with distance r at angle $\Theta = 0$ (left), $\Theta = \pi/4$ (middle), and $\Theta = \pi/2$ (right) and temperature $T = 1.5\,T_c$. We can observe that the potential and its variation are different in all three directions. Initially,

55

the potential increases sharply and then saturates as the distance increases. The potential decreases with an increase in velocity at a very short distance, whereas at a large distance, the potential increases as velocity increases; this switching is more noticeable in the $\Theta = \pi/2$ case in Fig. 3.1. At small velocities, the deviation of the potential from the static case ($v = 0$) is very small, but as the velocity becomes very high, a rapid shift in potential is observed. As distance r increases, the potential becomes positive, and this sign flipping happens quickly as velocity increases. This means the negative potential region is less for fast-moving heavy quarks, and the probability of quarkonia formation is less. Also, as we move from $\Theta = 0$ to $\Theta = \pi/2$, the potential becomes positive rather slowly. Similarly, Fig. 3.2 shows the imaginary part of the potential against r at the same parameters mentioned above. The imaginary potential is always negative, as expected, and its magnitude increases as velocity increases. The quarkonium potential is more sensitive to the velocity along the direction of motion, *i.e.,* at $\Theta = 0$.

Figure 3.3 illustrates the comparison between Cornell and Coulomb potential ($\sigma = 0$ case) along the heavy quark's motion direction. Both the real and imaginary parts of the Coulomb potential have nominal dependence on velocity, whereas the string part of the potential has substantial dependence on velocity from static to relativistic case. This implies the velocity dependence of the Cornell potential is almost solely due to the string part of the potential.

Figure 3.4 shows the angular dependence of the real (left) and imaginary (right) part of the potential at $r = 1$ fm and $T = 1.5\, T_c$, respectively. Both parts are symmetric about the plane containing the particle and perpendicular to the direction of motion. It is interesting to note that velocity dependence is most prominent along the direction of the velocity of heavy quarks for both real and imaginary parts of the potential. There is little variation in potential at low velocities, but as velocity increases, the spherical symmetry breaks down, leading to an increase in anisotropy. The real part is minimum, and the imaginary part is

maximum at $\Theta = \pi/2$ direction. Therefore, the quarkonia are most likely to be oriented in a plane perpendicular to its direction of motion.

In Fig. 3.5, we have made a comparison between velocity dependence and temperature dependence of the real part of the potential. It is interesting to note that the effect of velocity decreases with an increase in temperature in the case of the real part of the potential, especially at $\Theta = 0$, *i.e.,* the variation of potential with change in velocity is more at $T = 1.5\,T_c$ than $T = 2.5\,T_c$. In comparison to the static case, $v = 0$, the potential changes more at finite/high velocity with temperature. Our results show that the velocity dependence of the real part is as important as temperature dependence. Similarly, in Fig. 3.6, we compare velocity dependence and temperature dependence of the imaginary part of the potential. The potential variation with temperature at different angles and velocities is more or less the same. The potential changes rapidly along the direction of motion $\Theta = 0$ of the heavy quark than the perpendicular direction $\Theta = \pi/2$. Our results show that the heavy quark velocity and the medium temperature highly influence the quarkonium potential.

Figure 3.7 shows the variation of the thermal width with velocity (left) and temperature (right) of charmonium (J/Ψ) and bottomonium (Υ) ground states. Even though the magnitude of the imaginary part of the potential increases with velocity, the thermal width decreases with velocity due to the phenomenon of time dilation. Note that the thermal width obtained here qualitatively agrees with the thermal width calculated in Ref. [133] within the real-time formalism using the hard thermal loop approximation and also with results in Ref. [147] at the leading order in perturbative QCD. The width increases with temperature for both the charmonium and bottomonium states. The mass of the charm quark (taken $M_c = 1.27$ GeV) is less as compared to the bottom (taken $M_b = 4.18$ GeV), one can notice that the thermal width of J/Ψ is higher than Υ for the same parameters. This preserves the fact that the lighter bound state, *i.e., $c\bar{c}$* dissociates faster than the comparatively heavier one. The results clearly demonstrate the relevance and trends of velocity dependence

though the calculations used approximations and are only valid for deep-lying bound states corresponding to low temperatures. For the proper computation of the width, one must solve the 3D Schrodinger equation including both the real and imaginary parts and solve for the imaginary part of the eigenvalues.

Chapter 4

Quarkonia in QGP and magnetic field

Drawing upon the research conducted by Jobin Sebastian, Lata Thakur, Hiranmaya Mishra, and Najmul Haque, as presented in *Phys.Rev.D* **108** (2023), 094001.

This chapter explores the computation of the complex potential for heavy quarkonium in the context of relativistic heavy-ion collisions with an accompanying magnetic field. Initially, the one-loop gluon polarization tensor is derived using the Schwinger proper time formalism in Euclidean space, assuming a constant and homogeneous external magnetic field. With the obtained gluon polarization tensor, the gluon propagator is calculated, facilitating the determination of the dielectric permittivity in the presence of the magnetic field. The modified dielectric permittivity is then utilized to compute the complex potential for heavy quarkonia.

The results demonstrate the anisotropic nature of the heavy quarkonium potential, which depends on the angle between the $Q\bar{Q}$ dipole axis and the direction of the magnetic field. The chapter thoroughly discusses how the heavy quarkonium potential is influenced by the strength of the magnetic field and the angular orientation of the dipole. Additionally, the magnetic field influence on the thermal widths of quarkonium states is analyzed. Finally, the chapter examines the limitations of the strong-field approximation commonly employed in the literature related to heavy-ion observables, considering the nominal effect of the magnetic field on the quarkonium potential.

4.1 Context and Objectives

The presence of nonequilibrium effects, such as momentum space anisotropy due to viscous effects, bulk viscosity, moving medium, and magnetic fields [158, 159, 161–169, 220], can significantly impact the screening phenomenon, leading to in-medium modifications of quarkonium properties. Over the past decade, the properties of strongly interacting matter have garnered considerable interest, particularly in the presence of magnetic field backgrounds. Noncentral heavy-ion collision experiments at RHIC and LHC can generate a robust magnetic field normal to the reaction plane [82, 90, 91, 93, 170], motivating numerous phenomenological studies. These investigations have revealed novel phenomena, including magnetic catalysis [171–173], inverse magnetic catalysis [174, 175], chiral magnetic effects [176–181], splitting of open charm directed flow [83, 182–184], and modifications in the properties of heavy quarkonia and dynamics [185, 187–197]. The potential models have proven successful in describing quarkonium properties in both vacuum and medium conditions [112, 198–200]. The Cornell potential effectively captures quarkonium states, incorporating both perturbative Coulombic and nonperturbative confining terms [108, 109]. The emergence of an imaginary part of the potential in the presence of the medium [77, 124, 201–205] has prompted investigations into the heavy quarkonium complex potential [142, 206–210]. While lattice QCD has examined the real part of the quarkonium potential in a magnetic field background in both the vacuum and at finite temperature [211, 212], as of now, no lattice QCD study has explored the imaginary part of the heavy quarkonium potential.

This study aims to investigate the heavy quarkonium complex potential in the presence of a general magnetic field without imposing any restrictions on its strength. Previous examinations of the heavy quarkonium potential in magnetic fields focused on weak and strong field regimes [186–188]. A recent study by Ghosh et al. [185] considered the modification

of the imaginary part of the potential in the presence of a general magnetic field, demonstrating anisotropic behavior without discussing the real part. In this work, we compute both the real and imaginary parts of the complex heavy quarkonium potential in a constant magnetic field of arbitrary strength. Our approach utilizes the Schwinger proper time formalism to investigate the impact of an external constant magnetic field on both parts of the potential [213]. Additionally, we explore the effect of an arbitrary magnetic field on the thermal widths of heavy quarkonium states. This analysis is crucial as it considers the magnetic field generated in heavy-ion collisions, which may not necessarily be weak or strong compared to the temperature.

4.2   Permittivity in the presence of magnetic field

In this section, we develop the formulation for the dielectric permittivity under the influence of an arbitrary magnetic field—an essential component for calculating the in-medium heavy quarkonium potential. Initially, we conduct computations for the gluon self-energies and propagators, considering the impact of the arbitrary magnetic field.

4.2.1   Gluon self-energy in an arbitrary magnetic field

In the subsequent discussion, we revisit the calculation of the longitudinal component of the gluon self-energy at the one-loop level, following the approach outlined in Ref. [213]. We extract the longitudinal component of the gluon self-energy and propagator in the static limit, which corresponds to determining the Debye screening mass and gluon propagator in this limit. To set the context, let's consider a charged particle with charge q_f and mass m in the presence of an external, constant, and homogeneous magnetic field aligned along the

z-direction ($\mathbf{B} = B\hat{z}$). Here, we choose the symmetric gauge; therefore, we have

$$A_0(x) = 0, \quad A_1(x) = -\frac{B}{2}y,$$
$$A_2(x) = \frac{B}{2}x, \quad A_3(x) = 0. \tag{4.1}$$

In coordinate space, the fermion propagator, as introduced by Schwinger, is given by [214]

$$S(x, x') = e^{iex^\mu A_\mu(x')}\widetilde{S}(x - x'), \tag{4.2}$$

where the phase factor, $\Phi(x, x') = e^{iex^\mu A_\mu(x')}$, does not contribute to the gluon self-energy with this particular choice of the gauge Eq. (4.1); the self-energy is written in position space as follows

$$\Pi(x, x') = -g^2 \, \mathrm{tr}\left[\gamma^\mu s(x, x') \gamma^\nu s(x', x)\right]. \tag{4.3}$$

Therefore, we can write

$$\Pi(x, x') = -g^2 e^{i[\Phi(x, x') + \Phi(x', x)]} \, \mathrm{tr}\left[\gamma^\mu \widetilde{S}(x - x') \gamma^\gamma S(x' - x)\right]. \tag{4.4}$$

If the quark flavor f running in the loop remains the same, then $\Phi(x, x') + \Phi(x', x) = 0$. Noting that $\Pi(x, x')$ is translation invariant, one obtains $\Pi(x, x') = \Pi(x - x')$. Here, we note that for any closed fermion loop, the phase factor cancels, making the gluon polarization tensor a translation invariant irrespective of the choice of the gauge. Therefore, it is sufficient for our study to work with the translation invariant part of the propagator.

The Fourier transform $\widetilde{S}(k)$ of the translational invariant part of fermion propagator $\widetilde{S}(x - x')$ in the proper time formalism is

$$\widetilde{S}(k) = \int_0^\infty ds \, e^{is[k_0^2 - k_3^2 - k_\perp^2 \tan(|q_f B|s)/|q_f B|s - m^2]}$$
$$\times \{(k_0\gamma_0 - k_3\gamma_3 + m)[1 + \gamma_1\gamma_2 \tan(|q_f B|s)] - k_\perp\gamma_\perp[1 + \tan^2(|q_f B|s)]\}, \tag{4.5}$$

where $k_\perp = (k_1, k_2)$ is the transverse momentum. For the finite temperature case, we note that the bosonic Matsubara modes $\omega_n = 2n\pi T$ and fermionic ones $\hat{\omega}_l = (2l + 1)\pi T$,

respectively. The fermion propagator, in Euclidean space ($k_0 = i\hat{\omega}_l$) along with $s \to -is$ as followed in Ref. [213], becomes

$$
\widetilde{S}_l(\mathbf{k}) = -i \int_0^\infty ds\, e^{-s[\hat{\omega}_l^2 + k_3^2 + k_\perp^2 \tanh(|q_f B|s)/|q_f B|s + m^2]}
$$
$$
\times \left\{ (-\hat{\omega}_l \gamma_4 - k_3 \gamma_3 + m)[1 - i\gamma_1\gamma_2 \tanh(|q_f B|s)] - k_\perp \gamma_\perp [1 - \tanh^2(|q_f B|s)] \right\}, \quad (4.6)
$$

where $\mathbf{k} = (k_\perp, k_3)$ and $\gamma_\mu (\mu = 1, 2, 3, 4)$ are the Euclidean gamma matrices satisfy the anticommutation relation $\{\gamma_\mu, \gamma_\nu\} = -2\delta_{\mu\nu}$.

Based on the fermion propagator Eq. (4.6), one can obtain the quark-loop contribution to the one-loop gluon self-energy in the presence of a magnetic field as

$$
\Pi_n^{\mu\nu}(\mathbf{p}, B) = -g^2 T \sum_f \int \frac{d^3\mathbf{k}}{(2\pi)^3} \sum_{l=-\infty}^{\infty} \text{tr}\{\gamma^\mu \widetilde{S}_l(\mathbf{k})\gamma^\nu \widetilde{S}_{l-n}(\mathbf{k} - \mathbf{p})\} + Q^{\mu\nu}(p), \quad (4.7)
$$

where, with $p = |\mathbf{p}|$ and $Q^{\mu\nu}(p)$ is the "contact" term, which cancels the ultraviolet divergences and is independent of both the temperature and magnetic field. Our focus now lies on determining the longitudinal component of the gluon polarization tensor. This specific component is crucial for subsequent calculations involving the dielectric permittivity and, consequently, the in-medium heavy quarkonium potential. The longitudinal component of the quark contribution to the one-loop gluon self-energy is obtained after integration over $\mathbf{k}$ [213].

$$
\Pi_{n,q}^{44}(\omega_n, \mathbf{p}, B) = -\sum_f \frac{g^2 T}{8\pi^{3/2}} q_f B \int_0^\infty du\, u^{1/2} \int_{-1}^1 dv \sum_{l=-\infty}^{\infty}
$$
$$
\times \exp\left[\frac{p_\perp^2}{q_f B} \frac{\cosh(q_f Buv) - \cosh(q_f Bu)}{2\sinh q_f Bu} - u\left\{ m^2 + W_l^2 + \frac{1}{4}(1 - v^2)(\omega_n^2 + p_3^2) \right\} \right]
$$
$$
\times \left[\frac{p_\perp^2}{2} \frac{\cosh(q_f Buv) - v\coth(q_f Bu)\,\sinh(q_f Buv)}{\sinh(q_f Bu)} - \frac{1}{u}\coth(q_f Bu) \right.
$$
$$
\left. \times \left(1 - 2\,u\,W_l^2 + \frac{1}{2} u\,v\,\omega_n W_l - u(1 - v^2)p_3^2 \right) \right] + Q^{44}(p), \quad (4.8)
$$

where $W_l = \hat{\omega}_l - [(1 - v)/2]\omega_n$. The contact term $Q^{44}(p)$ is independent of temperature

and magnetic field and hence can be obtained as both T and B approaches zero.

By employing Poisson resummation, it is possible to separate the temperature-independent and temperature-dependent components of the longitudinal polarization tensor [213]. Since our focus is on investigating the influence of the magnetic field on the medium's heavy quark-antiquark potential, we exclusively address the temperature-dependent portion of the gluon self-energy. The temperature-dependent segment of the longitudinal polarization tensor in the limit of massless quarks is then discussed.

$$
\Pi_{n,q}^{44}(\omega_n, \boldsymbol{p}, B) = - \sum_f \frac{g^2}{(4\pi)^2} q_f B \int_0^\infty du \int_{-1}^1 dv \sum_{l \geq 1} (-1)^l
$$
$$
\times \exp\left[-\frac{p_\perp^2}{q_f B} \frac{\cosh(q_f Bu) - \cosh(q_f Buv)}{2\sinh(q_f B\, u)} - \frac{1}{4} u\left(1 - v^2\right)\left(p_3^2 + \omega_n^2\right) \right] e^{-\frac{l^2}{4T^2 u}}
$$
$$
\times \left[\cos(\pi ln(1-v)) \left\{ p_\perp^2 \frac{\cosh(q_f Buv) - v\coth(q_f Bu)\,\sinh(q_f Buv)}{\sinh(q_f Bu)} \right. \right.
$$
$$
\left. + \mathrm{p}_3^2\left(1 - v^2\right)\coth(q_f Bu) \right\} - \frac{\coth(q_f Bu)}{u}\left\{ \frac{l^2}{T^2 u}\cos \pi ln(1-v) - 2\pi\, l\, n\, v \sin \pi ln(1-v) \right\} \Bigg].
$$
$$
\tag{4.9}
$$

After evaluating the sum over l, the above Eq. (4.9) in the static limit becomes

$$
\Pi_q^{44}(0, \boldsymbol{p}, B) = \Pi_q^L(\boldsymbol{p}, B),
$$
$$
= \sum_f \frac{g^2}{32\pi^2} q_f B \int_0^\infty du \int_{-1}^1 dv \exp\left[-\frac{1}{4}p_3^2 u(1 - v^2) - \frac{p_\perp^2}{q_f B} \frac{\cosh(q_f Bu) - \cosh(q_f Buv)}{2\sinh(q_f Bu)} \right]
$$
$$
\times \left[4\coth q_f Bu \frac{\partial}{\partial u}\vartheta_4(0, e^{-\frac{1}{4T^2 u}}) + \left(1 - \vartheta_4\left(0, e^{-\frac{1}{4T^2 u}}\right)\right) \right.
$$
$$
\times \left\{ p_\perp^2 \frac{\cosh(q_f Buv)}{\sinh(q_f Bu)} + \coth(q_f Bu)\left(p_3^2 - p_3^2 v^2 - p_\perp^2 v \frac{\sinh(q_f Buv)}{\sinh(q_f Bu)}\right) \right\} \Bigg],
$$
$$
\tag{4.10}
$$

where ϑ_4 is the Jacobi Theta function and obtained as

$$
\sum_{l=1}^\infty (-1)^l e^{-al^2} = \frac{1}{2}\left[\vartheta_4(0, e^{-a}) - 1\right].
\tag{4.11}
$$

In spherical polar coordinates, Eq. (4.10) becomes

$$\Pi_q^L(\boldsymbol{p}, B) = \sum_f \frac{g^2 q_f B}{32\pi^2} \int_0^\infty du \int_{-1}^1 dv$$

$$\times \exp\left[-\frac{p^2 \cos^2\theta u(1-v^2)}{4} - \frac{p^2 \sin^2\theta(\cosh(q_f Bu) - \cosh(q_f Buv))}{2\, q_f B \sinh(q_f Bu)} \right]$$

$$\times \left[4\coth(q_f Bu)\, \frac{\partial}{\partial u}\vartheta_4(0, e^{-\frac{1}{4T^2 u}}) + \left\{ p^2 \sin^2\theta \cosh(q_f Buv)\mathrm{csch}(q_f Bu) \right.\right.$$

$$\left.\left. +p^2 \coth(q_f Bu)\left(\cos^2\theta(1-v^2) - v\,\sin^2\theta\, \frac{\sinh(q_f Buv)}{\sinh(q_f Bu)} \right) \right\} \left(1 - \vartheta_4(0, e^{-\frac{1}{4T^2 u}}) \right) \right].$$

$$(4.12)$$

Here the coupling constant g depends upon magnetic field, *i.e.,* $g^2(\Lambda^2, B) = 4\pi\alpha_s(\Lambda^2, B)$, where α_s is the one-loop running coupling constant in the magnetic field background as followed in [215, 216]

$$\alpha_s(\Lambda^2, |eB|) = \frac{\alpha_s(\Lambda^2)}{1 + b_1\alpha_s(\Lambda^2)\ln\left(\frac{\Lambda^2}{\Lambda^2 + |eB|}\right)}, \qquad (4.13)$$

and the one-loop strong coupling in the absence of any magnetic field is

$$\alpha_s(\Lambda^2) = \frac{1}{b_1\ln\left(\frac{\Lambda^2}{\Lambda_{\overline{\mathrm{MS}}}^2}\right)}, \qquad (4.14)$$

where $b_1 = \frac{(11N_c - 2N_f)}{12\pi}$ and $\Lambda_{\overline{\mathrm{MS}}} = 176$ MeV for $N_f = 3$. Here we take Λ for quarks as $\Lambda_q = 2\pi\sqrt{T^2 + \mu^2/\pi^2}$ and for gluons as $\Lambda_g = 2\pi T$. We take the zero chemical potential (μ) here. The quark loop contribution to the gluon self-energy, $\Pi_q^L(\boldsymbol{p})$ for $B = 0$ case can be written as

$$\Pi_q^L(\boldsymbol{p}) = -\frac{3\, g^2}{2\,\pi^2} \int_0^\infty \frac{k\, dk}{e^{k/T} + 1} \times \left[2 + \frac{(p^2 - 4k^2)}{2\, k\, p}\log\left(\frac{p - 2\, k}{p + 2\, k} \right) \right]. \qquad (4.15)$$

The magnetic field dependence only comes through the quark loop contribution to the gluon self-energy, as gluons do not interact with the magnetic field. Therefore, the gluon contribution to the self-energy remains the same as without the magnetic field.

$$\Pi_g^L(\omega, \boldsymbol{p}) = m_{Dg}^2\left[1 - \frac{\omega}{2p}\ln\left(\frac{\omega + p}{\omega - p} \right) + i\pi\frac{\omega}{2p}\Theta(p^2 - \omega^2) \right], \qquad (4.16)$$

where $m_{Dg}^2 = \frac{g'^2 T^2 N_c}{3}$ with $g'^2 = 4\pi\alpha_s(\Lambda^2)$ with $\alpha_s(\Lambda^2)$ defined in Eq. (4.14).

The above equation (4.16) can be rewritten in terms of real and imaginary parts as

$$
\begin{aligned}
\Re\Pi_g^L(\omega, \boldsymbol{p}) &= m_{Dg}^2\left[1 - \frac{\omega}{2p}\ln\left(\frac{\omega+p}{\omega-p}\right)\right], \\
\Im\Pi_g^L(\omega, \boldsymbol{p}) &= m_{Dg}^2\frac{\pi\omega}{2p}\Theta(p^2 - \omega^2).
\end{aligned}
\tag{4.17}
$$

The total longitudinal component of gluon self-energy is the sum of the gluon and quark contribution

$$
\Pi^L(\omega_n, \boldsymbol{p}, B) = \Pi_g^L(\omega_n, \boldsymbol{p}) + \Pi_q^L(\omega_n, \boldsymbol{p}, B),
\tag{4.18}
$$

which can be written in terms of real and imaginary parts. We compute the gluon self-energy's real and imaginary parts in the static limit ($\omega \to 0$). The real part of self-energy reads

$$
\Re\Pi^L(\omega, \boldsymbol{p}, B) = \Re\Pi_g^L(\omega, \boldsymbol{p}) + \Re\Pi_q^L(\omega, \boldsymbol{p}, B),
\tag{4.19}
$$

and the imaginary part of the self-energy $\Im\Pi^L$ reads

$$
\Im\Pi^L(\omega, \boldsymbol{p}, B) = \Im\Pi_g^L(\omega, \boldsymbol{p}) + \Im\Pi_q^L(\omega, \boldsymbol{p}, B).
\tag{4.20}
$$

The imaginary contribution from the quark loop can be obtained by using the identity

$$
\Im\Pi_{n,q}^L(\omega_n, \boldsymbol{p}) = \frac{1}{2i}\lim_{\varepsilon\to 0}\left[\Pi_q^L(\omega_n + i\varepsilon, \boldsymbol{p}) - \Pi_q^L(\omega_n - i\varepsilon, \boldsymbol{p})\right].
\tag{4.21}
$$

Further, we compute both the real and imaginary part of the longitudinal component of the gluon propagator using the gluon self-energy. The spectral function approach, as defined in Ref. [139], is used to obtain the imaginary part of the gluon propagator as

$$
\Im D^L(\omega, \boldsymbol{p}) = -\pi(1 + e^{-\beta\omega})\mathrm{A}^{\mathrm{L}},
\tag{4.22}
$$

where A^{L} is defined as

$$
\mathrm{A}^{\mathrm{L}}(\omega, \boldsymbol{p}) = \frac{1}{\pi}\frac{e^{\beta\omega}}{e^{\beta\omega} - 1}\rho^{\mathrm{L}}(\omega, \boldsymbol{p}).
\tag{4.23}
$$

The spectral function ρ^L can be expressed in the Breit-Wigner form as

$$\rho^L(\omega_n, \boldsymbol{p}, B) = \frac{\Im\Pi^L(\omega_n, \boldsymbol{p}, B)}{(p^2 - \Re\Pi^L(\omega_n, \boldsymbol{p}, B))^2 + \Im\Pi^L(\omega_n, \boldsymbol{p}, B)^2}, \tag{4.24}$$

where $p = |\boldsymbol{p}|$. After substituting Eq. (4.24) in Eq. (4.22), we obtain the longitudinal component of the gluon propagator, D^L in terms of real and imaginary parts. In the static $(\omega \to 0)$ and massless light quark limit, we obtain

$$D^L(\boldsymbol{p}, B) = \frac{-1}{p^2 + \Pi^L(\boldsymbol{p}, B)} + \frac{i\pi T \, \Pi^L(\boldsymbol{p}, B)}{p(p^2 + \Pi^L(\boldsymbol{p}, B))^2}. \tag{4.25}$$

Using the gluon propagator, we obtain the dielectric permittivity as [136, 141, 186]

$$\epsilon^{-1}(\boldsymbol{p}, B) = \frac{p^2}{p^2 + \Pi^L} - i\pi T \frac{p\,\Pi^L}{(p^2 + \Pi^L)^2}, \tag{4.26}$$

where $\Pi^L \equiv \Pi^L(\boldsymbol{p}, B)$.

We use the dielectric permittivity expression (4.26) to compute the in-medium heavy quarkonium complex potential in an arbitrary magnetic field.

4.3   In-medium heavy quarkonium potential

This section is dedicated to deriving the in-medium heavy quarkonium potential, incorporating the effects of a magnetized thermal medium. It is worth to note here that quarkonium states do not have a conserved center-of-mass momentum in an external magnetic field. Instead there is a new conserved quantity called the pseudomomentum which takes into account the Lorentz force on the particles in the system [219, 220]. The correction to the Cornell potential in Fourier space is achieved by multiplying it with the dielectric permittivity, as previously computed [132, 133, 141].

$$V(\boldsymbol{r}, T, B) = \int \frac{d^3\boldsymbol{p}}{(2\pi)^{3/2}} \left(e^{i\boldsymbol{p}\cdot\boldsymbol{r}} - 1\right) \frac{V_{\text{Cornell}}(p)}{\epsilon(p, B)}, \tag{4.27}$$

where $V_{\text{Cornell}}(p)$ is the Fourier transform of the Cornell potential $V_{\text{Cornell}}(r) = -\alpha/r + \sigma\, r$, which is given by

$$V_{\text{Cornell}}(p) = \sqrt{\frac{2}{\pi}}\frac{\alpha}{p^2} - 2\sqrt{\frac{2}{\pi}}\frac{\sigma}{p^4}, \tag{4.28}$$

where α and σ are the strong coupling constant and the string tension, respectively. Here
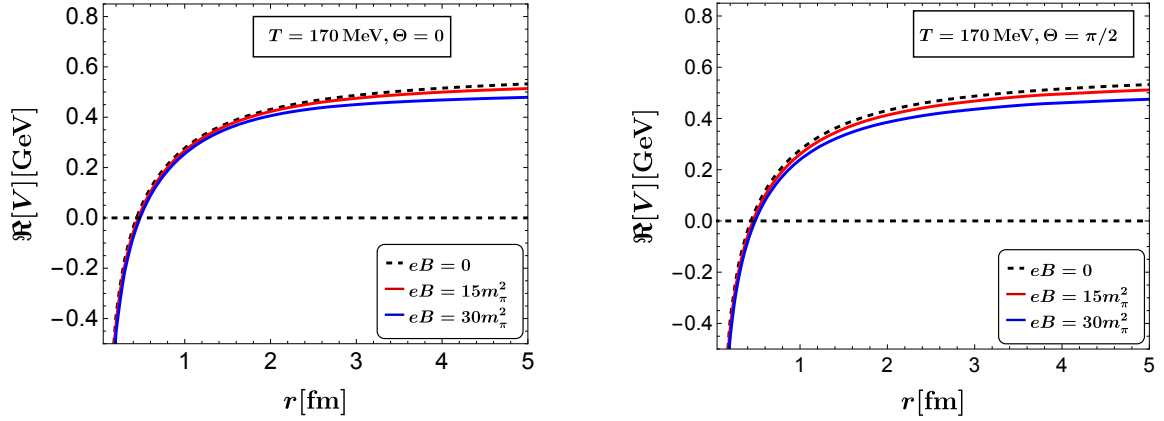
Figure 4.1: The real part of the potential as a function of the separation r between the quark and antiquark for $\Theta = 0$ (left) and $\Theta = \pi/2$ (right) at $T = 170$ MeV.
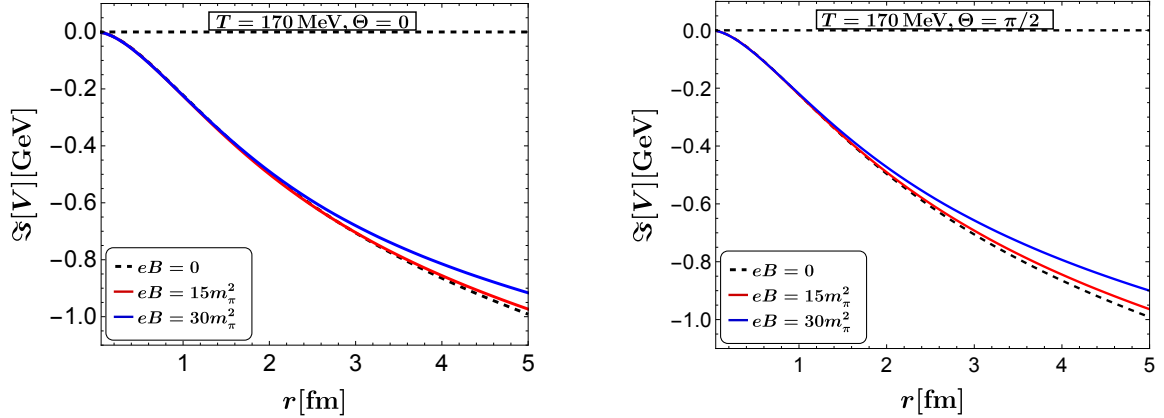
Figure 4.2: The imaginary part of the potential is depicted as a function of the separation r between the quark and antiquark for $\Theta = 0$ (left) and $\Theta = \pi/2$ (right) at $T = 170$ MeV.

we take $\alpha = 4/3\,\alpha_s(\Lambda^2, B)$ and $\sigma = 0.18\,\text{GeV}^2$ and $\epsilon(p)$ is the dielectric permittivity, which is defined in Eq. (4.26). After substituting Eqs. (4.26) and (4.28) in Eq. (3.11), we obtain both the real as well as imaginary part of the potential, which contains both the perturbative
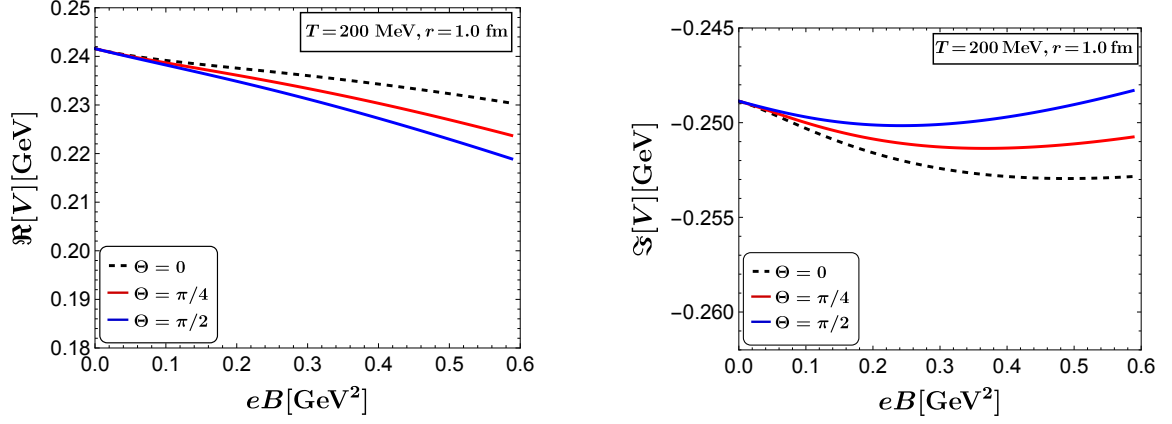
Figure 4.3: The complex potential is shown as a function of magnetic field strength for different values of Θ when $r = 1$ fm and $T = 200$ MeV. The left panel illustrates the variation of the real part of the potential, while the right panel displays the variation of the imaginary part of the potential.

Coulombic and nonperturbative string terms. The real part of the potential can be written in terms of Coulombic and string terms as

$$\Re V(\boldsymbol{r}, T, B) = \Re V_c(\boldsymbol{r}, T, B) + \Re V_\sigma(\boldsymbol{r}, T, B), \tag{4.29}$$

where the Coulombic term is

$$\Re V_c(\boldsymbol{r}, T, B) = -\frac{\alpha}{2\pi^2} \int d^3\boldsymbol{p} \left[\frac{e^{i\boldsymbol{p}\cdot\boldsymbol{r}}}{p^2 + \Pi^L} - \frac{\Pi^L}{p^2(p^2 + \Pi^L)} \right], \tag{4.30}$$

and the string term reads

$$\Re V_\sigma(\boldsymbol{r}, T, B) = -\frac{\sigma}{\pi^2} \int \frac{d^3\boldsymbol{p}}{(2\pi)^3} (e^{i\boldsymbol{p}\cdot\boldsymbol{r}} - 1) \frac{1}{p^2(p^2 + \Pi^L)}. \tag{4.31}$$

Here $\boldsymbol{p} \cdot \boldsymbol{r} = rp\big[\sin\theta \sin\Theta \cos(\phi - \Phi) + \cos\theta \cos\Theta\big]$ and the angles $\theta(\Theta)$ and $\phi(\Phi)$ are polar and azimuthal angles in momentum (coordinate) space, respectively. After integrating over the azimuthal angle, we obtain

$$\Re V(r, T, B, \Theta) = -\frac{1}{\pi} \int \frac{\sin\theta \, d\theta \, dp}{p^2 + \Pi^L} \Big[(\alpha \, \Pi^L - 2\,\sigma)$$
$$\times (\alpha \, p^2 + 2\,\sigma) e^{ipr\cos\theta\cos\Theta} J_0(pr\sin\theta\sin\Theta) \Big], \tag{4.32}$$

69

where J_0 is the Bessel's function of the first kind.

Similarly, we compute the imaginary part of the quarkonium potential. The imaginary part of the potential is given by

$$\Im V(\boldsymbol{r}, T, B) = T \int \frac{d^3\boldsymbol{p}}{2\pi} \frac{(e^{i\boldsymbol{p}\cdot\boldsymbol{r}} - 1)\Pi^L p}{(p^2 + \Pi^L)^2} \left[\frac{\alpha}{p^2} + \frac{2\sigma}{p^4}\right]. \tag{4.33}$$

After integrating over the azimuthal angle, we obtain

$$\Im V(r, \Theta, T, B) = -T \int \frac{\sin\theta \, d\theta \, dp}{(p^2 + \Pi^L)^2} \Pi^L \left[\alpha p + \frac{2\sigma}{p}\right] \left\{1 - e^{ipr\cos\theta\cos\Theta} J_0(pr\sin\theta\sin\Theta)\right\}. \tag{4.34}$$

We numerically solve the real (4.32) and imaginary (4.34) parts of the potential. In Fig. 4.1,
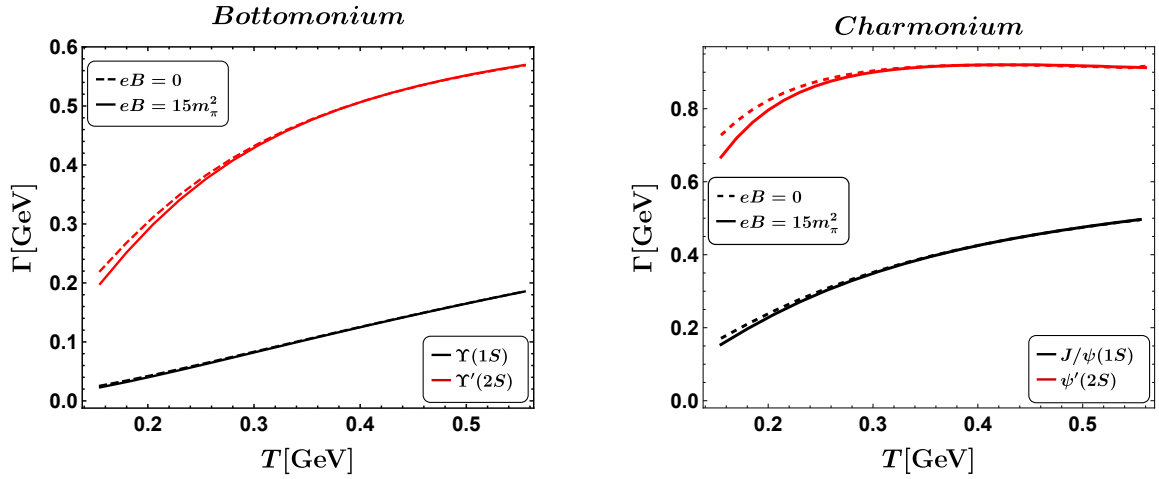
Figure 4.4: The thermal widths of bottomonium (left) and charmonium (right) states as functions of temperature at $B = 0$ and $15m_\pi^2$ are presented.

we plot the real part of the potential as a function of separation distance r for different magnetic field strengths eB. The left panel shows the $Q\bar{Q}$ dipole axis alignment along the direction of the magnetic field ($\Theta = 0$), whereas the right panel shows its perpendicular alignment with respect to the magnetic field ($\Theta = \pi/2$). We find that the real part of the potential becomes flattened with the magnetic field due to an increase in screening with B. The effect of screening is seen to be slightly higher in the perpendicular case than along the direction of the magnetic field.

In Fig. 4.2, we plot the the imaginary part of the potential for $\Theta = 0$ (left) and $\Theta = \pi/2$ (right) for the different values of the magnetic field. The imaginary part of the potential shows different behavior at smaller and larger r; it increases with the magnetic field at smaller r and decreases in magnitude with the increase in the magnetic field at larger r. The decrease in magnitude with the magnetic field is observed to be higher for $\Theta = \pi/2$ compared to $\Theta = 0$. Note that the magnetic field dependence is insignificant for the potential, especially in the range $eB = 0$ to $eB = 15m_\pi^2$.

Figure 4.3 shows the potential's real and imaginary parts as a magnetic field function for different Θ values at $r = 1$ fm. We observe that the real part of the potential varies in response to a magnetic field at different rates according to direction. The magnetic field dependence is found to be maximum in the $\Theta = \pi/2$ direction and minimum along the direction of the magnetic field, which establishes the anisotropy of the potential in the magnetic field. The magnitude of the imaginary part of the potential initially increases with the magnetic field and decreases as the field intensifies. While both components of the potential exhibit some dependence on the magnetic field magnitude and angle, this dependency is relatively weak.

The next section utilizes the imaginary part of the potential to derive the thermal widths of the quarkonium states.

4.4   Thermal Width

In this section, we calculate the thermal widths of the quarkonium states by treating the imaginary part of the potential as a perturbation of the vacuum potential. The decay width, $\Gamma_{Q\bar{Q}}$, for the quarkonium states is computed as [141, 142]

$$\Gamma_{Q\bar{Q}}(T, B) = -\langle \psi(r) | \Im V_{Q\bar{Q}}(r, T, B, \Theta) | \psi(r) \rangle, \tag{4.35}$$

71
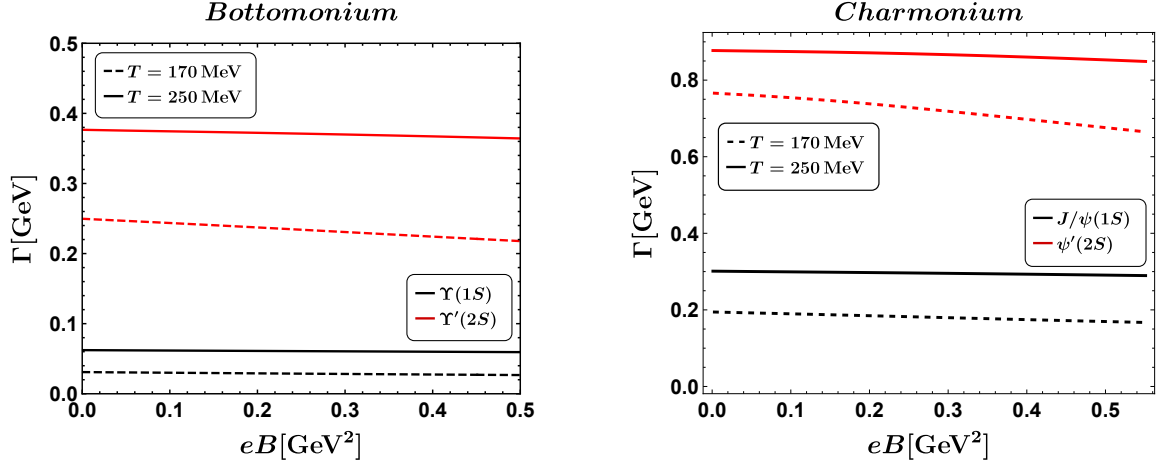
Figure 4.5: Thermal widths of bottomonium (left) and charmonium (right) states as a function of magnetic field for $T = 170$ MeV and 250 MeV.

where $\psi(r)$ is the unperturbed Coulombic wave function. The use of Coulomb wave functions is justified as the leading contribution to the imaginary potential for a deeply bound heavy-quark state is Coulombic. The wave functions for the ground and excited states are expressed as

$$\begin{aligned}
\psi_{1s}(r) &= \frac{1}{(\pi a_0^3)^{1/2}} e^{-r/a_0}, \\
\psi_{2s}(r) &= \frac{1}{4(2\pi a_0^3)^{1/2}} \left(2 - \frac{r}{a_0}\right) e^{-r/2a_0},
\end{aligned} \tag{4.36}$$

where $a_0 = 2/C_F m_Q \alpha_s$ is the Bohr radius of the $Q\bar{Q}$ system and m_Q is the heavy quark mass. After substituting Eqs. (4.36) and (4.34) in Eq. (4.35), we obtain the thermal width of the quarkonium states for the ground state as

$$\begin{aligned}
\Gamma_{1s}(T, B) &= -\frac{1}{\pi a_0^3} \int d^3\mathbf{r}\, e^{-2r/a_0} \Im V\left(r, T, B, \Theta\right), \\
&= \frac{2T}{a_0^3} \int dr\, d\Theta\, r^2 \sin\Theta e^{-2r/a_0} \int \frac{\sin\theta\, d\theta\, dp}{(p^2 + \Pi^L)^2} \Pi^L \left[\alpha p + \frac{2\sigma}{p}\right], \quad (4.37)
\end{aligned}$$

and for the first excited states $(2S)$ as

$$\Gamma_{2s}(T, B) = \frac{T}{16a_0^3} \int dr\, d\Theta\, r^2 \sin\Theta \left(2 - \frac{r}{a_0}\right)^2 e^{-r/a_0} \int \frac{\sin\theta\, d\theta\, dp}{(p^2 + \Pi^L)^2} \Pi^L \left[\alpha p + \frac{2\sigma}{p}\right]. \quad (4.38)$$

We numerically compute the thermal widths of the ground (4.37) and excited (4.38) states of the bottomonium and charmonium states. In Fig. 4.4, we present plots of the thermal widths of the ground and first excited states of bottomonium (on the left) and charmonium (on the right) as a function of temperature for both $eB = 0$ and $eB = 15m_\pi^2$.

It is observed that the thermal width increases with an increase in temperature, as anticipated. The magnetic field effect is more pronounced on the first excited state than the ground state for both the bottomonium and charmonium states. The effect of the magnetic field on the imaginary part of the potential is more significant due to the larger size of the excited states. Hence, the excited states are more sensitive to the magnetic field than the ground state. Figure 4.5 illustrates the variation of thermal width with the magnetic field at different temperatures for bottomonium (left) and charmonium (right) states. We find that the thermal widths are more sensitive to the magnetic field at lower temperatures than at higher temperatures. The magnetic field effects decrease with the increase in heavy quark mass and decrease in the size of bound states. It can be concluded from the figures that the magnetic field has only a negligible effect on the thermal width compared to the temperature.

4.5 Strong field approximation

In this section, we compute the longitudinal component of the gluon self-energy in the strong magnetic field approximation ($T \ll \sqrt{|eB|}$). In the strong magnetic field limit ($|eB| \to \infty$), the fermion propagator [Eq. (4.6)] for massless case becomes

$$
\begin{aligned}
\widetilde{S}_l(\mathbf{k}) &= -i \int_0^\infty ds \, e^{-s[\hat{\omega}_l^2 + k_3^2 + k_\perp^2/|q_f B|s]}(-\hat{\omega}_l\gamma_4 - k_3\gamma_3)[1 - i\gamma_1\gamma_2], \\
&= ie^{-k_\perp^2/|q_f B|}\frac{\hat{\omega}_l\gamma_4 + k_3\gamma_3}{\hat{\omega}_l^2 + k_3^2}[1 - i\gamma_1\gamma_2], \quad (4.39)
\end{aligned}
$$

which is similar to the expression for the fermion propagator computed for the lowest Landau level approximation in Refs. [217,218]. In $|eB| \to \infty$ limit, the temperature-dependent
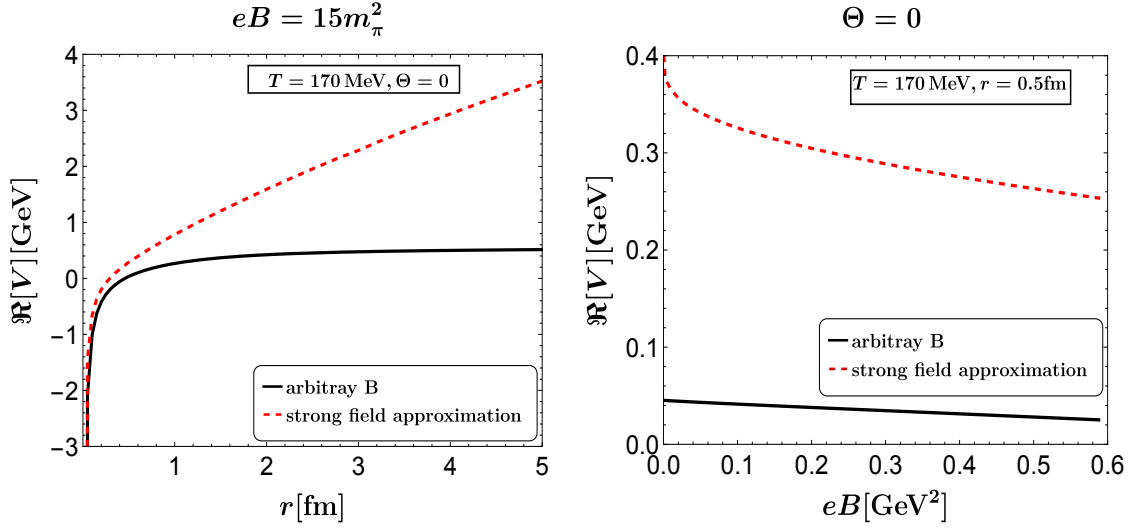
Figure 4.6: The real part of the potential as a function of r is plotted on the left side for an arbitrary (black solid) and strong magnetic field approximation (red dashed) at $T = 170$ MeV and $\Theta = 0$. The right side depicts the same potential as a function of eB at $r = 0.5$ fm.

part of the longitudinal component of the gluon self-energy (4.9) reduces to the dominant term as

$$
\begin{aligned}
\Pi_q^L(\omega_n, \mathbf{p}, B) &= -\sum_f \frac{g^2}{(4\pi)^2} \frac{(q_f B)^2}{T^2} e^{-p_\perp^2/2q_f B} \int_0^\infty \frac{du}{u^2} \\
&\times \int_{-1}^1 dv\, e^{-cu} \sum_{l \geq 1} (-1)^{(l+1)} l^2 e^{-d/u} \cos \pi ln(1-v),
\end{aligned}
\tag{4.40}
$$

where $c = (1-v^2)(p_3^2 + \omega_n^2)/(4\,q_f B)$ and $d = l^2 q_f B/4T^2$. The integration over u can be done analytically using the relation

$$
\int_0^\infty \frac{du}{u^2} e^{-cu-d/u} = 2\sqrt{\frac{c}{d}} K_1(2\sqrt{c\,d}).
\tag{4.41}
$$

Here $K_n(z)$ represents the modified Bessel function of the second kind. Therefore, the longitudinal component of the gluon self-energy (4.40) for the strong magnetic field ap-

proximation in the static limit ($\omega_n \to 0$) becomes

$$\Pi_q^L(\boldsymbol{p}, B) = -\sum_f \frac{g^2 q_f B}{8\pi^2 T} e^{-p_\perp^2/2q_f B} \sum_{l \geq 1} (-1)^{(l+1)}$$

$$\times \int_{-1}^{1} dv\, l\, p_3 \sqrt{1-v^2} K_1 \left(\frac{l\, p_3}{2T} \sqrt{1-v^2} \right). \tag{4.42}$$

Further, we compute the Debye screening mass from Eq. (4.9) in the limit $p \to 0$, for the regime where $T \ll \sqrt{eB}$

$$
\begin{aligned}
m_D^2(T, B) &= -\lim_{\boldsymbol{p} \to 0} \Pi_q^L(\boldsymbol{p}, B), \\
&= \sum_f \frac{g^2 q_f B}{8\pi^2 T^2} \int_0^\infty \frac{du}{u^2} \coth q_f B\, u \sum_{l \geq 1} (-1)^{l+1} l^2 e^{-l^2/4uT^2}, \\
&= \sum_f \frac{g^2 q_f B}{4\pi^2}.
\end{aligned}
\tag{4.43}
$$

In the absence of a magnetic field, the Debye screening mass becomes

$$
\begin{aligned}
m_D^2(T) &= \frac{1}{3} C_A g^2 T^2 + \sum_f \frac{g^2}{8\pi^2 T^2} \int_0^\infty \frac{du}{u^3} \sum_{l \geq 1} (-1)^{l+1} l^2 e^{-l^2/4uT^2}, \\
&= \frac{1}{3} C_A g^2 T^2 + \frac{1}{6} N_f g^2 T^2.
\end{aligned}
\tag{4.44}
$$

The longitudinal component of gluon self-energy in strong field approximation obtained in Eq. (4.42) can be substituted in Eq. (3.11) to study the behavior of quarkonium potential in the strong field approximation. In Fig. 4.6, we show the effect of arbitrary magnetic fields and the strong field approximation on the real part of the potential. We find that the real part of the potential is more suppressed in the case of an arbitrary magnetic field compared to the strong field approximation due to larger screening in an arbitrary B. It is evident that the potential with the approximation differs significantly for large magnetic field magnitudes from the exact potential, and this difference gradually reduces as the magnetic field increases. Hence, we can conclude that the strong field approximation is invalid, and one should consider the general case when studying the properties of quarkonium states.

Chapter 5

Summary and Conclusions

The QGP produced in heavy-ion collisions undergoes a hydrodynamic expansion, cools down, and eventually transforms into hadron gases. Since the final observables related to hadrons provide insights into the entire evolution of the system, it is crucial to develop comprehensive dynamic models that can accurately describe each stage of these collisions. The standard methodology for modeling heavy-ion collisions involves an initial-state model followed by applying hydrodynamic expansion and, subsequently, a hadronic cascade. This methodology ensures a holistic understanding of the complex processes occurring during heavy-ion collisions, allowing researchers to interpret experimental results and gain deeper insights into the behavior of matter under extreme conditions. The QGP produced in these experiments is distinguished by its remarkably compact dimensions, typically 10fm, and its exceedingly transient nature, with a fleeting existence of just around 10^{-23} S. Given the exceptionally brief persistence of the QGP medium that emerges in high-energy heavy-ion collisions, it presents a formidable set of challenges for quantitative property analysis.

Due to the higher masses, quarkonia are mostly created at the very early stages after the collisions and behave more or less as an independent degree of freedom while passing through the various phases of the created matter. However, they are slightly affected by the QGP medium while passing through it, resulting in distinctive signatures in their final yields observed at the detectors. In the context of this thesis, it is important to highlight that the investigation of heavy quarkonia serves as one of the initial and pivotal signals proposed for scrutinizing the QGP generated through heavy-ion collisions. In the realm of quarko-

nium research, potential models have exhibited remarkable success in characterizing these particles, whether they exist in a vacuum or within a medium. At the forefront of these models is the Cornell potential, as detailed in references [108, 109]. The Cornell potential, endowed with both perturbative Coulombic and non-perturbative confining elements, offers a robust framework for accurately describing quarkonium states. Furthermore, the advent of an imaginary component in the potential has catalyzed investigations into the intricate domain of complex potentials governing heavy quarkonium [77, 124]. Beyond these technical merits, Cornell potential has played an indispensable role in advancing our comprehension of various aspects of heavy quarkonia.

This thesis investigated two significant scenarios that could lead to anisotropy in the heavy quarkonium potential. These scenarios arise from the relative motion between the quarkonium and the QGP medium and a strong magnetic field in the noncentral collision that is normal to the reaction plane. In the rapidly expanding QGP, the dynamic Debye screening of heavy quarkonium is important as the quark-antiquark potential depends on the velocity of the quarkonia in the medium. This is the motivation to study the velocity dependence of the potential and the modifications of quarkonium-bound states, which becomes relevant in a relativistically expanding medium. The velocity dependence was brought into the picture through the concept of retarded potential. The thesis undertook a comprehensive analysis of the effects of temperature, velocity, and screening on the retarded potential of moving quarkonia in the static medium of QGP, including its angular dependence during motion. Additionally, the study utilized the imaginary part of the potential to estimate the thermal width of quarkonia and explored its dependence on velocity and temperature. Another significant aspect addressed in the thesis was the influence of a magnetic field on the heavy quarkonium complex potential, allowing for a general magnetic field without restricting its strength. Through the Schwinger proper time formalism, the research investigated the impact of an arbitrary magnetic field on both the real and imaginary

parts of the complex heavy quarkonium potential, along with a discussion on its effects on the thermal widths of heavy quarkonium states.

In Chapter 3, the study focused on the potential of a moving heavy quarkonium in a static QGP medium. Initially, the retarded potential of a uniformly moving heavy quark in the vacuum was derived, drawing an analogy to the Liénard-Wiechert potential in electrodynamics. This involved performing Lorentz transformations on the static potential to express its form in a boosted frame. Subsequently, the velocity and angular-dependent potential were adjusted to incorporate the screening effect of the QGP medium. This adjustment was made through the medium dielectric permittivity, resulting in a complex potential. The chapter presented both exact numerical results and derived analytical expressions in the small velocity limit for both the real and imaginary parts of the potential. Various parameters, including the distance between quark-antiquark, temperature, velocity, and angular dependence, were explored through plots illustrating the potential variation.

Furthermore, a comparison between the Coulombic and Cornell potentials, accounting for the presence or absence of string terms, was provided. As anticipated, the Coulombic contribution prevailed at short distances, while the string term dominated at larger quarkonium separation distances. The study also revealed that the motion of quarkonium through the QGP disrupts the spherical symmetry of the potential, with an increasing anisotropy in the potential observed as velocity rises. Notably, the velocity dependence of the potential was established to be equally significant as the temperature dependence. The maximum variation in both the real and imaginary parts of the potential from the corresponding static case was found to align with the direction of quarkonium motion. Lastly, the thermal width was computed, showing a decrease with velocity and an increase with temperature. This insight suggests that the lifetime of a quarkonium-bound state is influenced by both the velocity of the quarkonium and the temperature of the medium. The real part of the potential was observed to turn positive rapidly as distance increased with velocity, particularly pro-

78

nounced in the direction of quarkonium motion, leading to the contraction and deformation of the Debye sphere.

Continuing from the current study, the next step would involve utilizing the potential derived in this chapter to delve into the dynamics of heavy quarkonia propagation within the QGP medium. The calculation of the binding energy can be accomplished by solving the Schrödinger equation, making use of the real part of the potential. It is anticipated that the velocity and angular dependence of the potential will play a crucial role in modifying the survival probabilities of quarkonia, warranting further investigation in this direction.

In Chapter 4, the impact of a magnetic field on the heavy quarkonium complex potential was examined. Initially, the dielectric permittivity was computed from the static limit of the gluon propagator. This propagator was derived from the one-loop gluon self-energy in the presence of an external magnetic field using Schwinger proper time formalism in Euclidean space. The magnetic field's influence was introduced through the quark-loop contribution to the gluon self-energy and the coupling constant. Later, the in-medium heavy quarkonium complex potential was computed using the modified dielectric permittivity. The results highlighted the anisotropic nature of this potential, showcasing variations with magnetic field strength and the angle Θ between the quark-antiquark axis and the magnetic field direction. For very high magnetic field strengths, the real part of the potential exhibited flattening due to increased screening with eB. Conversely, the imaginary part of the quarkonium potential displayed an initial increase in magnitude at short distances followed by a decrease at long distances. Additionally, the inclusion of a magnetic field introduced angular dependence on the potential. Ultimately, it was observed that the overall effect of the magnetic field on the complex potential remained relatively small for realistic strengths of the magnetic field generated in heavy-ion collisions.

The decay widths of the ground and first excited states of bottomonium (Υ, Υ') and charmonium $(J/\psi, \psi')$ were computed using the imaginary part of the potential. It was

observed that the excited states (Υ', ψ') are more sensitive to magnetic fields than the ground states (Υ, J/ψ). The sensitivity to magnetic fields decreases with increasing heavy quark mass and decreasing size, making the charmonium states more responsive to magnetic field strength than the bottomonium states. As temperature increases, the effect of magnetic fields on decay widths diminishes, eventually disappearing at high temperatures.

A comparison with the strong-field approximated potential revealed significant deviations. The strong-field approximated potential did not align with the potential without such an approximation for any realistic magnetic field value generated in heavy-ion collisions. The approximation resulted in weaker screening compared to the estimation for an arbitrary magnetic field, and this screening gradually increased with magnetic field strength. This investigation challenged the validity of the strong magnetic field approximation commonly employed in the literature for the heavy quarkonium complex potential. Considering the effects of a general magnetic field, as explored in this study, becomes essential for realistic strengths of magnetic fields. Additionally, it was noted that the weak-field expansion introduces new divergences in gluon propagators, necessitating regulation. The gluon propagator with momentum K in a weak field, *i.e.,* $\sqrt{|eB|} < (T \sim K)$, can be written up to $\mathcal{O}\left[(eB)^2\right]$ as (See the Ref. [218] for details)

$$
\begin{aligned}
S_m^w(K) =& \frac{\slashed{K}}{K^2} + \frac{q_f B \left(\gamma_5\{(K\cdot n)\slashed{u} - (K\cdot u)\slashed{n}\}\right)}{K^4} \\
&+ 2\left(q_f B\right)^2 \left[\frac{\{(K\cdot u)\slashed{u} - (K\cdot n)\slashed{n}\} - \slashed{K}}{K^6} - \frac{k_\perp^2 \slashed{K}}{K^8}\right] + \mathcal{O}\left[(eB)^3\right],
\end{aligned}
$$

where u_μ is the four-velocity of the heat bath and n_μ is associated with the electromagnetic field tensor and represents the direction of the magnetic field. Note that $\mathcal{O}(eB^0)$ term is $\sim 1/K$, whereas $\mathcal{O}(eB^2)$ term is $\sim 1/K^3$. So, the weak field expansion introduces an extra infrared divergence in the computation. To avoid the infrared divergence, an arbitrary strength of magnetic field is used in the thesis and also future work aims to extend this computation to a moving medium in the presence of an arbitrary magnetic field.

80

References

[1] D. J. Gross and F. Wilczek, *Phys. Rev. D* **8**, 3633-3652 (1973).

[2] D. J. Gross and F. Wilczek, *Phys. Rev. Lett.* **30**, 1343-1346 (1973).

[3] H. D. Politzer, *Phys. Rev. Lett*. **30**, 1346-1349 (1973).

[4] M. Gell-Mann, *Phys. Rev.* **125**, 1067-1084 (1962).

[5] V. E. Barnes, *et al. Phys. Rev. Lett.* **12**, 204-206 (1964).

[6] O. W. Greenberg, *Phys. Rev. Lett.* **13**, 598-602 (1964).

[7] M. Y. Han and Y. Nambu, *Phys. Rev.* **139**, B1006-B1010 (1965).

[8] M. Gell-Mann, *Physics Physique Fizika* **1**, 63-75 (1964).

[9] M. Breidenbach, *et al. Phys. Rev. Lett.* **23**, 935-939 (1969).

[10] E. D. Bloom, *et al. Phys. Rev. Lett.* **23**, 930-934 (1969).

[11] J. D. Bjorken, *Phys. Rev.* **179**, 1547-1553 (1969).

[12] C. G. Callan, Jr. and D. J. Gross, *Phys. Rev. Lett.* **22**, 156-159 (1969).

[13] K. G. Wilson, *Phys. Rev.* **179**, 1499-1512 (1969).

[14] I. B. Khriplovich, *Sov. J. Nucl. Phys.* **10**, 235-242 (1969).

[15] G. 't Hooft, *Nucl. Phys. B* **35**, 167-188 (1971).

[16] G. 't Hooft, *Nucl. Phys. B* **33**, 173-199 (1971).

[17] C. N. Yang and R. L. Mills, *Phys. Rev.* **96**, 191-195 (1954).

[18] H. Fritzsch, M. Gell-Mann and H. Leutwyler, *Phys. Lett. B* **47**, 365-368 (1973).

[19] K. G. Wilson, *Phys. Rev. D* **10**, 2445-2459 (1974).

[20] J. B. Kogut, *Rev. Mod. Phys.* **51**, 659 (1979).

[21] M. Creutz, *Phys. Rev. D* **21**, 2308-2315 (1980).

[22] J. B. Kogut and L. Susskind, *Phys. Rev. D* **11**, 395-408 (1975).

[23] J. J. Aubert *et al.* [E598], *Phys. Rev. Lett.* **33**, 1404-1406 (1974).

[24] J. E. Augustin *et al.* [SLAC-SP-017], *Phys. Rev. Lett.* **33**, 1406-1408 (1974).

[25] T. Appelquist and H. D. Politzer, *Phys. Rev. Lett.* **34**, 43 (1975).

[26] S. W. Herb *et al.* [E288], *Phys. Rev. Lett.* **39**, 252-255 (1977).

[27] F. Abe *et al.* [CDF], *Phys. Rev. Lett.* **74**, 2626-2631 (1995).

[28] S. Abachi *et al.* [D0], *Phys. Rev. Lett.* **74**, 2632-2637 (1995).

[29] R. Brandelik *et al.* [TASSO], *Phys. Lett. B* **86**, 243-249 (1979).

[30] C. Berger *et al.* [PLUTO], *Phys. Lett. B* **86**, 418-425 (1979).

[31] W. Bartel *et al.* [JADE], *Phys. Lett. B* **91**, 142-147 (1980).

[32] G. Hanson *et al.*, *Phys. Rev. Lett.* **35**, 1609-1612 (1975).

[33] D. P. Barber *et al. Phys. Rev. Lett.* **43**, 830 (1979).

[34] Y. Nambu and G. Jona-Lasinio, *Phys. Rev.* **122**, 345-358 (1961).

[35] R. D. Pisarski and F. Wilczek, *Phys. Rev. D* **29**, 338-341 (1984).

[36] S. Bethke, *Prog. Part. Nucl. Phys.* **58**, 351-386 (2007).

[37] F. Wilczek, *Rev. Mod. Phys.* **71**, S85-S95 (1999).

[38] D. J. Gross, *Proc. Nat. Acad. Sci.* **102**, 9099-9108 (2005).

[39] J. Goldstone, A. Salam and S. Weinberg, *Phys. Rev.* **127**, 965-970 (1962).

[40] G. T. Bodwin, E. Braaten and G. P. Lepage, *Phys. Rev. D* **51**, 1125-1171 (1995).

[41] S. Muroya, A. Nakamura, C. Nonaka and T. Takaishi, *Prog. Theor. Phys.* **110**, 615-668 (2003).

[42] C. Ratti, *Rept. Prog. Phys.* **81**, 084301 (2018).

[43] N. Cabibbo and G. Parisi, *Phys. Lett. B* **59**, 67-69 (1975).

[44] E. V. Shuryak, *Sov. Phys. JETP* **47**, 212-219 (1978). IYF-77-34.

[45] A. Bazavov *et al.* [HotQCD], *Phys. Rev. D* **90**, 094503 (2014).

[46] A. Aprahamian *et al.* "Reaching for the horizon: The 2015 long range plan for nuclear science."

[47] E. Annala, T. Gorda, A. Kurkela, J. Nättilä and A. Vuorinen, *Nature Phys.* **16**, 907-910 (2020).

[48] L. Evans and P. Bryant, *JINST* **3**, S08001 (2008).

[49] W. Busza, K. Rajagopal and W. van der Schee, *Ann. Rev. Nucl. Part. Sci.* **68**, 339-376 (2018).

[50] [ALICE], [arXiv:2211.04384 [nucl-ex]].

[51] H. Song and U. W. Heinz, *Phys. Rev. C* **78**, 024902 (2008).

[52] P. Romatschke, *Eur. Phys. J. C* **52**, 203-209 (2007).

[53] K. Aamodt *et al.* [ALICE], *Phys. Rev. Lett.* **106**, 032301 (2011).

[54] S. Ryu *et al. Phys. Rev. Lett.* **115**, 132301 (2015).

[55] G. Denicol, A. Monnai and B. Schenke, *Phys. Rev. Lett.* **116**, 212301 (2016).

[56] L. Adamczyk *et al.* [STAR], *Phys. Rev. C* **92**, 014904 (2015).

[57] W. Zhao, W. Ke, W. Chen, T. Luo and X. N. Wang, *Phys. Rev. Lett.* **128**, 022302 (2022).

[58] X. N. Wang, *Nucl. Phys. A* **750**, 98-120 (2005).

[59] M. Gyulassy and M. Plumer, *Phys. Lett. B* **243**, 432-438 (1990).

[60] R. Baier, Y. L. Dokshitzer, A. H. Mueller, S. Peigne and D. Schiff, *Nucl. Phys. B* **483**, 291-320 (1997).

[61] B. G. Zakharov, *JETP Lett.* **65**, 615-620 (1997).

[62] M. G. Mustafa and M. H. Thoma, *Acta Phys. Hung. A* **22**, 93-102 (2005).

[63] S. S. Adler *et al.* [PHENIX], *Phys. Rev. Lett.* **96**, 032301 (2006).

[64] S. Ghosh and V. Chandra, *Phys. Rev. D* **98**, 076006 (2018).

[65] [CMS], CMS-PAS-EXO-18-004, (2018).

[66] J. D. Bjorken and H. Weisberg, *Phys. Rev. D* **13**, 1405 (1976).

[67] J. Rafelski and B. Muller, *Phys. Rev. Lett.* **48**, 1066 (1982).

[68] P. Koch, B. Muller and J. Rafelski, *Phys. Rept.* **142**, 167-262 (1986).

[69] P. Koch, B. Muller and J. Rafelski, *Z. Phys. A* **324**, 453-463 (1986). UCT-TP-38-1986.

[70] J. Rafelski, *Phys. Lett. B* **262**, 333-340 (1991).

[71] E. Andersen *et al.* [WA97], *Phys. Lett. B* **449**, 401-406 (1999).

[72] S. V. Afanasiev *et al.* [NA49], *Phys. Rev. C* **66**, 054902 (2002).

[73] C. Alt *et al.* [NA49], *Phys. Rev. C* **77**, 024903 (2008).

[74] N. Brambilla *et al. Eur. Phys. J. C* **71**, 1534 (2011).

[75] T. Matsui and H. Satz, *Phys. Lett. B* **178**, 416-422 (1986).

[76] S. Digal, P. Petreczky and H. Satz, *Phys. Rev. D* **64**, 094015 (2001).

[77] M. Laine, O. Philipsen, P. Romatschke and M. Tassler, *JHEP* **03**, 054 (2007).

[78] R. L. Thews, M. Schroedter and J. Rafelski, *Phys. Rev. C* **63**, 054905 (2001).

[79] K. Zhou, N. Xu, Z. Xu and P. Zhuang, *Phys. Rev. C* **89**, 054911 (2014).

[80] A. Capella *et al. Eur. Phys. J. C* **58**, 437-444 (2008).

[81] L. Maiani, F. Piccinini, A. D. Polosa and V. Riquer, *Nucl. Phys. A* **748**, 209-225 (2005).

[82] V. Skokov, A. Y. Illarionov and V. Toneev, *Int. J. Mod. Phys. A* **24**, 5925-5932 (2009).

[83] J. Adam *et al.* [STAR], *Phys. Rev. Lett.* **123**, 162301 (2019).

[84] W. T. Deng and X. G. Huang, *Phys. Lett. B* **742**, 296-302 (2015).

[85] S. Chatterjee and P. Tribedy, *Phys. Rev. C* **92**, 011902 (2015).

[86] V. Voronyuk, V. D. Toneev, S. A. Voloshin and W. Cassing, *Phys. Rev. C* **90**, 064903 (2014).

[87] Y. Hirono, M. Hongo and T. Hirano, *Phys. Rev. C* **90**, 021903 (2014).

[88] J. Bloczynski, X. G. Huang, X. Zhang and J. Liao, *Nucl. Phys. A* **939**, 85-100 (2015).

[89] X. G. Huang, *Rept. Prog. Phys.* **79**, 076302 (2016).

[90] W. T. Deng and X. G. Huang, *Phys. Rev. C* **85**, 044907 (2012).

[91] A. Bzdak and V. Skokov, *Phys. Lett. B* **710**, 171-174 (2012).

[92] J. Bloczynski, X. G. Huang, X. Zhang and J. Liao, *Phys. Lett. B* **718**, 1529-1535 (2013).

[93] K. Tuchin, *Adv. High Energy Phys.* **2013**, 490495 (2013).

[94] U. Gursoy, D. Kharzeev and K. Rajagopal, *Phys. Rev. C* **89**, 054905 (2014).

[95] J. Adams *et al.* [STAR], *Nucl. Phys. A* **757**, 102-183 (2005).

[96] K. Adcox *et al.* [PHENIX], *Nucl. Phys. A* **757**, 184-283 (2005).

[97] B. B. Back *et al.* [PHOBOS], *Nucl. Phys. A* **757**, 28-101 (2005).

[98] I. Arsene *et al.* [BRAHMS], *Nucl. Phys. A* **757**, 1-27 (2005).

[99] J. Prakash, M. Kurian, S. K. Das and V. Chandra, *Phys. Rev. D* **103**, 094009 (2021).

[100] F. Prino and R. Rapp, *J. Phys. G* **43**, 093002 (2016).

[101] G. Montagnoli and A. M. Stefanini, *Eur. Phys. J. A* **53**, 169 (2017).

[102] A. Dumitru, Y. Guo and M. Strickland, *Phys. Lett. B* **662**, 37-42 (2008).

[103] H. Satz, *J. Phys. G* **32**, R25 (2006).

[104] H. T. Ding *et al.* PoS **LATTICE2010**, 180 (2010).

[105] G. Aarts *et al. Phys. Rev. Lett.* **106**, 061602 (2011).

[106] J. Beringer *et al.* [Particle Data Group], *Phys. Rev. D* **86**, 010001 (2012).

[107] A. Mocsy, P. Petreczky and M. Strickland, *Int. J. Mod. Phys. A* **28**, 1340012 (2013).

[108] E. Eichten *et al. Phys. Rev. Lett.* **34**, 369-372 (1975).

[109] E. Eichten, K. Gottfried, T. Kinoshita, K. D. Lane and T. M. Yan, *Phys. Rev. D* **21**, 203 (1980).

[110] G. X. A. Petronilo *et al. Int. J. Mod. Phys. A* **36**, 2150121 (2021).

[111] A. Vega and J. Flores, *Pramana* **87**, 73 (2016).

[112] F. Karsch, M. T. Mehr and H. Satz, *Z. Phys. C* **37**, 617 (1988).

[113] A. Mocsy and P. Petreczky, *Eur. Phys. J. C* **43**, 77-80 (2005).

[114] C. Y. Wong, *Phys. Rev. C* **72**, 034906 (2005).

[115] A. Mocsy and P. Petreczky, *Phys. Rev. D* **73**, 074007 (2006).

[116] D. Cabrera and R. Rapp, *Phys. Rev. D* **76**, 114506 (2007).

[117] A. Mocsy and P. Petreczky, *Phys. Rev. Lett.* **99**, 211602 (2007).

[118] W. M. Alberico, A. Beraudo, A. De Pace and A. Molinari, *Phys. Rev. D* **77**, 017502 (2008).

[119] A. Mocsy, *Eur. Phys. J. C* **61**, 705-710 (2009).

[120] F. Karsch, M. G. Mustafa and M. H. Thoma, *Phys. Lett. B* **497**, 249-258 (2001).

[121] M. Asakawa and T. Hatsuda, *Phys. Rev. Lett.* **92**, 012001 (2004).

[122] S. Datta, F. Karsch, P. Petreczky and I. Wetzorke, *Phys. Rev. D* **69**, 094507 (2004).

[123] G. Aarts, C. Allton, M. B. Oktay, M. Peardon and J. I. Skullerud, *Phys. Rev. D* **76**, 094513 (2007).

[124] A. Beraudo, J. P. Blaizot and C. Ratti, *Nucl. Phys. A* **806**, 312-338 (2008).

[125] M. Y. Jamal, I. Nilima, V. Chandra and V. K. Agotiya, *Phys. Rev. D* **97**, 094033 (2018).

[126] V. K. Agotiya, V. Chandra, M. Y. Jamal and I. Nilima, *Phys. Rev. D* **94**, 094006 (2016).

[127] M. A. Escobedo, J. Soto and M. Mannarelli, *Phys. Rev. D* **84**, 016008 (2011).

[128] M. A. Escobedo, F. Giannuzzi, M. Mannarelli and J. Soto, *Phys. Rev. D* **87**, 114005 (2013).

[129] H. Liu, K. Rajagopal and U. A. Wiedemann, *Phys. Rev. Lett.* **98**, 182301 (2007).

[130] P. Chakraborty, M. G. Mustafa and M. H. Thoma, *Phys. Rev. D* **74**, 094002 (2006).

[131] E. Caceres, M. Natsuume and T. Okamura, *JHEP* **10**, 011 (2006).

[132] V. Agotiya, V. Chandra and B. K. Patra, *Phys. Rev. C* **80**, 025210 (2009).

[133] L. Thakur, N. Haque and H. Mishra, *Phys. Rev. D* **95**, 036014 (2017).

[134] Y. Guo, L. Dong, J. Pan and M. R. Moldes, *Phys. Rev. D* **100**, 036011 (2019).

[135] D. Lafferty and A. Rothkopf, *Phys. Rev. D* **101**, 056010 (2020).

[136] L. Thakur, N. Haque, U. Kakade and B. K. Patra, *Phys. Rev. D* **88**, 054022 (2013).

[137] Y. Burnier, O. Kaczmarek and A. Rothkopf, *JHEP* **12**, 101 (2015).

[138] Y. Burnier, O. Kaczmarek and A. Rothkopf, *Phys. Rev. Lett.* **114**, 082001 (2015).

[139] H. A. Weldon, *Phys. Rev. D* **42**, 2384-2387 (1990).

[140] J. P. Blaizot and E. Iancu, *Phys. Rept.* **359**, 355-528 (2002).

[141] L. Thakur, U. Kakade and B. K. Patra, Phys. Rev. D **89** (2014), 094020.

[142] A. Dumitru, Y. Guo and M. Strickland, *Phys. Rev. D* **79**, 114003 (2009).

[143] M. G. Mustafa, M. H. Thoma and P. Chakraborty, *Phys. Rev. C* **71**, 017901 (2005).

[144] M. Laine and Y. Schroder, *JHEP* **03**, 067 (2005).

[145] N. Haque, A. Bandyopadhyay, J. O. Andersen, M. G. Mustafa, M. Strickland and N. Su, *JHEP* **05**, 027 (2014).

[146] A. Dumitru, Y. Guo, A. Mocsy and M. Strickland, *Phys. Rev. D* **79**, 054019 (2009).

[147] T. Song, Y. Park, S. H. Lee and C. Y. Wong, *Phys. Lett. B* **659**, 621-627 (2008).

[148] K. Bitaghsir Fadafan and S. K. Tabatabaei, *J. Phys. G* **43**, 095001 (2016).

[149] Q. Du, A. Dumitru, Y. Guo and M. Strickland, *JHEP* **01**, 123 (2017).

[150] L. Thakur, N. Haque and Y. Hirono, *JHEP* **06**, 071 (2020).

[151] L. Thakur and Y. Hirono, *JHEP* **02**, 207 (2022).

[152] A. Islam, L. Dong, Y. Guo, A. Rothkopf and M. Strickland, *EPJ Web Conf.* **274**, 04015 (2022).

[153] L. Dong, Y. Guo, A. Islam, A. Rothkopf and M. Strickland, *JHEP* **09**, 200 (2022).

[154] M. Singh, M. Kurian, S. Jeon and C. Gale, *Phys. Rev. C* **108**, 054901 (2023).

[155] J. Sebastian, M. Y. Jamal and N. Haque, *Phys. Rev. D* **107**, 054040 (2023).

[156] S. Chakraborty and N. Haque, *Nucl. Phys. B* **874**, 821-851 (2013).

[157] B. K. Patra, H. Khanchandani and L. Thakur, *Phys. Rev. D* **92**, 085034 (2015).

[158] J. Adam *et al.* [ALICE], *Phys. Rev. Lett.* **116**, 222301 (2016).

[159] K. Marasinghe and K. Tuchin, *Phys. Rev. C* **84**, 044908 (2011).

[160] J. Alford and M. Strickland, *Phys. Rev. D* **88**, 105017 (2013).

[161] C. S. Machado, F. S. Navarra, E. G. de Oliveira, J. Noronha and M. Strickland, *Phys. Rev. D* **88**, 034009 (2013).

[162] S. Cho, K. Hattori, S. H. Lee, K. Morita and S. Ozaki, *Phys. Rev. Lett.* **113**, 172301 (2014).

[163] X. Guo, S. Shi, N. Xu, Z. Xu and P. Zhuang, *Phys. Lett. B* **751**, 215-219 (2015).

[164] T. Yoshida and K. Suzuki, *Phys. Rev. D* **94**, 074043 (2016).

[165] A. V. Sadofyev and Y. Yin, *JHEP* **01**, 052 (2016).

[166] C. Bonati *et al. Phys. Rev. D* **95**, 074515 (2017).

[167] C. Bonati, M. D'Elia and A. Rucci, *Phys. Rev. D* **92**, 054014 (2015).

[168] R. Rougemont, R. Critelli and J. Noronha, *Phys. Rev. D* **91**, 066001 (2015).

[169] D. Dudal and T. G. Mertens, *Phys. Rev. D* **91**, 086002 (2015).

[170] D. E. Kharzeev, L. D. McLerran and H. J. Warringa, *Nucl. Phys. A* **803**, 227-253 (2008).

[171] V. P. Gusynin, V. A. Miransky and I. A. Shovkovy, *Phys. Rev. Lett.* **73**, 3499-3502 (1994).

[172] F. Bruckmann, G. Endrodi and T. G. Kovacs, *JHEP* **04**, 112 (2013).

[173] B. Chatterjee, H. Mishra and A. Mishra, *Phys. Rev. D* **84**, 014016 (2011).

[174] G. S. Bali, F. Bruckmann, G. Endrodi, Z. Fodor, S. D. Katz and A. Schafer, *Phys. Rev. D* **86**, 071502 (2012).

[175] A. Bandyopadhyay and R. L. S. Farias, *Eur. Phys. J. ST* **230**, no.3, 719-728 (2021).

[176] G. S. Bali, F. Bruckmann, G. Endrodi, F. Gruber and A. Schaefer, *JHEP* **04**, 130 (2013).

[177] V. Voronyuk *et al. Phys. Rev. C* **83**, 054911 (2011).

[178] K. Fukushima, D. E. Kharzeev and H. J. Warringa, *Phys. Rev. D* **78**, 074033 (2008).

[179] B. Alver and G. Roland, *Phys. Rev. C* **81**, 054905 (2010).

[180] M. Kurian, S. Mitra, S. Ghosh and V. Chandra, *Eur. Phys. J. C* **79**, 134 (2019).

[181] R. Ghosh, B. Karmakar and M. Golam Mustafa, *Phys. Rev. D* **103**, 074019 (2021).

[182] S. K. Das, S. Plumari, S. Chatterjee, J. Alam, F. Scardina and V. Greco, *Phys. Lett. B* **768**, 260-264 (2017).

[183] S. Acharya *et al.* [ALICE], *Phys. Rev. Lett.* **125**, 022301 (2020).

[184] K. K. Gowthama, M. Kurian and V. Chandra, *Phys. Rev. D* **103**, 074017 (2021).

[185] R. Ghosh, A. Bandyopadhyay, I. Nilima and S. Ghosh, *Phys. Rev. D* **106**, 054010 (2022).

[186] B. Singh, L. Thakur and H. Mishra, *Phys. Rev. D* **97**, 096011 (2018).

[187] M. Hasan, B. Chatterjee and B. K. Patra, *Eur. Phys. J. C* **77**, 767 (2017).

[188] M. Hasan and B. K. Patra, *Phys. Rev. D* **102**, 036020 (2020).

[189] G. Huang, J. Zhao and P. Zhuang, *Phys. Rev. D* **107**, 114035 (2023).

[190] J. Zhao, K. Zhou, S. Chen and P. Zhuang, *Prog. Part. Nucl. Phys.* **114**, 103801 (2020).

[191] A. Mishra and S. P. Misra, *Phys. Rev. C* **102**, 045204 (2020).

[192] Y. Chen, X. L. Sheng and G. L. Ma, *Nucl. Phys. A* **1011**, 122199 (2021).

[193] S. Iwasaki, M. Oka and K. Suzuki, *Eur. Phys. J. A* **57**, 222 (2021).

[194] K. Fukushima, K. Hattori, H. U. Yee and Y. Yin, *Phys. Rev. D* **93**, 074028 (2016).

[195] M. Kurian, V. Chandra and S. K. Das, *Phys. Rev. D* **101**, 094024 (2020).

[196] M. Kurian, S. K. Das and V. Chandra, *Phys. Rev. D* **100**, 074003 (2019).

[197] I. Nilima, A. Bandyopadhyay, R. Ghosh and S. Ghosh, *Eur. Phys. J. C* **83**, 30 (2023).

[198] W. Lucha, F. F. Schoberl and D. Gromes, *Phys. Rept.* **200**, 127-240 (1991).

[199] N. Brambilla, A. Pineda, J. Soto and A. Vairo, *Rev. Mod. Phys.* **77**, 1423 (2005).

[200] P. K. Srivastava, O. S. K. Chaturvedi and L. Thakur, *Eur. Phys. J. C* **78**, 440 (2018).

[201] M. Laine, O. Philipsen and M. Tassler, *JHEP* **09**, 066 (2007).

[202] Y. Burnier, M. Laine and M. Vepsalainen, *JHEP* **01**, 043 (2008).

[203] N. Brambilla, J. Ghiglieri, A. Vairo and P. Petreczky, *Phys. Rev. D* **78**, 014017 (2008).

[204] N. Brambilla, M. A. Escobedo, J. Ghiglieri and A. Vairo, *JHEP* **12**, 116 (2011).

[205] N. Brambilla, M. A. Escobedo, J. Ghiglieri and A. Vairo, *JHEP* **05**, 130 (2013).

[206] M. Margotta, K. McCarty, C. McGahan, M. Strickland and D. Yager-Elorriaga, *Phys. Rev. D* **83**, 105019 (2011).

[207] A. Rothkopf, T. Hatsuda and S. Sasaki, *Phys. Rev. Lett.* **108**, 162001 (2012).

[208] Y. Burnier and A. Rothkopf, *Phys. Rev. D* **86**, 051503 (2012).

[209] Y. Burnier and A. Rothkopf, *Phys. Lett. B* **753**, 232-236 (2016).

[210] A. Rothkopf, *Phys. Rept.* **858**, 1-117 (2020).

[211] C. Bonati *et al. Phys. Rev. D* **98**, 054501 (2018).

[212] C. Bonati *et al. Phys. Rev. D* **94**, 094007 (2016).

[213] J. Alexandre, *Phys. Rev. D* **63**, 073010 (2001).

[214] J. S. Schwinger, *Phys. Rev.* **82**, 664-679 (1951).

[215] A. Ayala *et al. Phys. Rev. D* **98**, 031501 (2018).

[216] A. Bandyopadhyay, B. Karmakar, N. Haque and M. G. Mustafa, *Phys. Rev. D* **100**, 034031 (2019).

[217] V. P. Gusynin, V. A. Miransky and I. A. Shovkovy, *Nucl. Phys. B* **462**, 249-290 (1996).

[218] B. Karmakar, A. Bandyopadhyay, N. Haque and M. G. Mustafa, *Eur. Phys. J. C* **79**, 658 (2019).

[219] J. Avron, I. Herbs, B. Simon, Annals Phys. 114 (1978) 431 doi:10.1016/0003-4916(78)90276-2

[220] J. Alford and M. Strickland, Phys. Rev. D **88** (2013), 105017 doi:10.1103/PhysRevD.88.105017 [arXiv:1309.3003 [hep-ph]].